Analysis of the 3–7 October 2000 and 15–24 April 2002 geomagnetic storms with an optimized nonlinear dynamical model

E. Spencer,[1] W. Horton,[2] M. L. Mays,[2] I. Doxas,[3] and J. Kozyra[4]

Received 14 August 2006; revised 10 November 2006; accepted 7 December 2006; published 28 April 2007.

[1] A computationally optimized low-dimensional nonlinear dynamical model of the magnetosphere-ionosphere system called WINDMI is used to analyze two large geomagnetic storm events, 3–7 October 2000 and 15–24 April 2002. These two important storms share common features such as the passage of magnetic clouds, shock events from coronal mass ejections, triggered substorms, and intervals of sawtooth oscillations. The sawtooth oscillations resemble periodic substorms but occur in association with strong or building ring current populations and have injection regions that are unusually close to the Earth and unusually wide in magnetic local times (Henderson et al., 2006; Borovsky et al., 2007). The April 2002 event includes one of the best examples of sawtooth events ever observed. On 18 April 2002, sawtooth oscillations were clearly visible when solar wind conditions (IMF B_z, density, pressure) were relatively steady with a slowly varying *Dst*. In this study, WINDMI is used to model the 3–7 October 2000 and 15–24 April 2002 geomagnetic activity. WINDMI results are evaluated focusing on the sawtooth intervals and the overall prediction of the westward auroral electrojet (*AL*) index and *Dst* index. The input to the model is the dynamo driving voltage derived from the fluctuating solar wind plasma and the interplanetary magnetic field measured by the ACE satellite. The output of the model is a field-aligned current proportional to the *AL* index and the energy stored in the ring current which is proportional to the *Dst* index. The model parameters are optimized using a genetic algorithm (GA) to obtain solutions that simultaneously have least mean square fit to the *AL* and *Dst* indices and also exhibit substorms of period 2–4 hours. The GA optimization results show that the model is able to predict the *Dst* index reliably and captures the timing and periodicity of the sawtooth signatures in the *AL* index reasonably well for both storm events.

Citation: Spencer, E., W. Horton, M. L. Mays, I. Doxas, and J. Kozyra (2007), Analysis of the 3–7 October 2000 and 15–24 April 2002 geomagnetic storms with an optimized nonlinear dynamical model, *J. Geophys. Res.*, *112*, A04S90, doi:10.1029/2006JA012019.

1. Introduction

[2] Two geomagnetic storms of contemporary interest are the large events of 3–7 October 2000 and 15–24 April 2002 which occurred during the recent solar maximum. *Wang et al.* [2003] reports coronal mass ejection (CME) induced interplanetary (IP) shocks in the 3–7 October 2000 period. Similarly, during the 15–24 April 2002 geomagnetic storm, the Solar and Heliospheric Observatory (SOHO) detected three CME-induced IP shocks [*Gopalswamy et al.*, 2002]. The increased solar wind activity caused by these IP shocks was measured by the Advanced Composition Explorer (ACE) satellite and the ground-based *AL* and *Dst* index measurements.

[3] Both storm periods also record the passage of a magnetic cloud (MC), during which global sawtooth oscillations are detected. Sawtooth oscillations have been observed during magnetic cloud events with modest values ($B_z^{IMF} \sim -10$ nT), when solar wind conditions are slowly varying and relatively weak. Conditions on 4 October 2000 and 18 April 2002 are typical of those that produce sawtooth events. The sawtooth oscillations resemble periodic substorms but the injection boundary tends to occur unusually close to Earth, over a broader range of magnetic local times, and with a more extreme dipolarization of the magnetic field than for more typical substorms [*Henderson*, 2004; *Henderson et al.*, 2006; *Borovsky et al.*, 2007].

[1] Center for Space Engineering, Utah State University, Logan, Utah, USA.
[2] Institute for Fusion Studies, University of Texas at Austin, Austin, Texas, USA.
[3] Center for Integrated Plasma Studies, University of Colorado, Boulder, Colorado, USA.
[4] Department of Atmospheric, Oceanic and Space Sciences, University of Michigan, Ann Arbor, Michigan, USA.

0148-0227/07/2006JA012019

[4] An interesting aspect of the sawtooth oscillations is that they occur during solar wind flows with low Alfvénic Mach numbers (i.e., modest B_z^{IMF} with low solar wind densities), conditions that tend to occur within coronal mass ejections. These conditions have been associated with saturation of the polar cap potential and with unusually strong convection in the magnetosphere [*Borovsky et al.*, 2007]. The signature of sawtooth events have been noted in the ring current ENA populations, strongest in the oxygen component (discussed by *Henderson et al.* [2006]). Sawtooth events are also associated with low plasma sheet densities (ring current source population). When sawtooth injections appear at geosynchronous orbit a small recovery of order 10 nT can sometimes be seen in the Sym-H index. This recovery is likely due to the disruption of the magnetotail currents close to Earth as the magnetic field dipolarizes. Small recoveries of Sym-H associated with each dipolarization are clearly seen on 18 April 2002 [*Henderson et al.*, 2006]. (The Sym-H index is another measure of the severity of magnetic storms and is similar to the *Dst*. Here we use the *Dst* index and defer consideration of Sym-H to another study. The difference is not important for this work.)

[5] In this work a computationally optimized nonlinear dynamical model of the coupled magnetosphere-ionosphere system called WINDMI [*Doxas et al.*, 2004; *Horton et al.*, 2005a] is used to analyze both these important geomagnetic storms and to capture some of the important events that occur within them. The WINDMI model simulates through a physics network, the energy transfer into, and between dominant components of the nightside magnetosphere and ionosphere. Maintaining energy balance between global components of the Magnetosphere-Ionosphere-Ring Current (M-I-RC) system results in a low-dimensional (d = 8) nonlinear system of ordinary differential equations that are solved numerically to determine the state of every component. The output of the model is a region 1 field-aligned current (R1 FAC) and the energy stored in the ring current which are compared to the *AL* and *Dst* indices, respectively.

[6] Determination of the various dynamical quantities is based on the geometry of the Tsyganenko magnetic field model [*Tsyganenko and Usmanov*, 1982] of the Earth's magnetosphere. The magnetosphere is partitioned into five regions: (1) the geotail lobe, (2) the central plasma sheet, (3) the ring current, (4) the nightside region 1 current, and (5) the nightside region 2 current closing as a partial ring current. The basic energy components associated with these regions of the nightside magnetosphere are (1) the lobe magnetic energy, (2) the plasma thermal energy, (3) the parallel streaming kinetic energy due to plasma flow along magnetic field lines, and (4) the cross-tail kinetic energy due to plasma flow perpendicular to the magnetic field. These components channel energy to the ionosphere via the nightside region-1 currents [*Horton and Doxas*, 1996; *Horton and Doxas*, 1998]. The region-1 current is then proportional to the *AL* index measured by ground-based stations. The two largest energy components in the model are (1) the magnetic energy W_m stored in the geotail lobes that extend to a distance L_x behind the Earth and (2) the plasma energy $W_{\rm rc}$ in the ring current.

[7] The model has been improved [*Doxas et al.*, 2004] and includes the energy of the ring current plasma driven by plasma injection across the Alfvén layer in the nightside inner magnetotail transition region. The ring current plasma energy is a new component of the model that leads to the predicted *Dst* index through the Dessler-Parker-Sckopke relation [*Dessler and Parker*, 1959; *Sckopke*, 1966]. A limitation of the model is that the physical dimensions of the regions are constrained to be time invariant. The parameters of the model are coefficients of the differential equations that relate to plasma properties and physical dimensions of the magnetosphere-ionosphere system. These parameters are estimated using physical considerations or measured data.

[8] In an earlier work, *Horton et al.* [2003] used the WINDMI model to classify three types of substorms based on (1) a bimodal response with an internal trigger based on the near-Earth neutral line model, (2) a rapid unloading initiated by a northward turning of the IMF, and (3) a linear filter response. With this framework, the WINDMI model successfully reproduced three types of substorms [*Horton et al.*, 2003] in a database with 117 isolated substorms [*Blanchard and McPherron*, 1993].

[9] In the work of *Horton et al.* [2005b], set of parameters obtained through manual estimation of the conditions in the nightside magnetosphere was used to obtain good results in the analysis of the 3–7 October 2000 storm. In this work a genetic algorithm optimization procedure is employed to tune the model computationally, using a combination of cost functions to extract physically acceptable solutions from the parameter search space that fit well to the measured *AL* and *Dst* indices as well as exhibit periodic substorms and other phenomena of interest especially with respect to the *AL* index. In order to select solutions that meet multiple criteria in an independent way, a multiobjective optimization scheme is used to obtain the best parameters. The optimal solution is selected through a qualitative assessment of a family of pareto-optimal parameter sets that are returned by the optimization algorithm. The computational method employed here will form the basis of an automated real-time *AL* and *Dst* prediction model to be developed in the future.

[10] In section 2 we present the satellite and ground-based data for both the storm periods and discuss some important features of each event. In section 3 we describe the data derived signal that is used as the input into the WINDMI model. In section 4 we present the WINDMI model in some detail and compare the WINDMI results with *AL* and *Dst* indices using nominal parameters in subsection 4.2. In section 5 a brief explanation of the genetic algorithm based optimization method will be given. In section 6 we will discuss and compare the WINDMI results obtained through the optimization procedure with the data. Finally, we will summarize and draw some conclusions about the performance of the WINDMI model in section 7. We also include additional details of the single and multiobjective optimization algorithm in Appendix A.

2. Storm Data

[11] Complete measurements of solar wind proton density, solar wind velocity and the Interplanetary Magnetic Field (IMF) in GSM coordinates for the two geomagnetic storm periods are available from the Advanced Composition Explorer (ACE) satellite. We use these quantities to derive

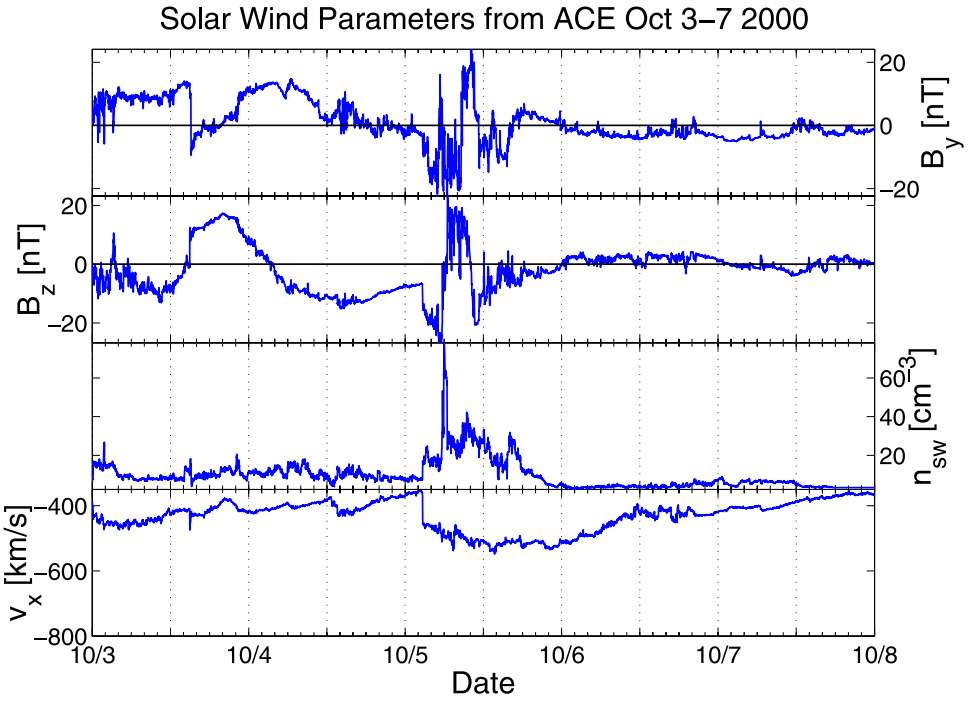

Figure 1. ACE satellite measurement of the solar wind velocity v_x, proton density n_{sw}, B_z^{IMF}, and B_y^{IMF} components for 3–7 October 2000, in GSM coordinates. The satellite was located at approximately $X = 224$, $Y = -29$, $Z = -5$ Earth radii in GSM coordinates during this period.

an input dynamo voltage for the WINDMI model. In addition, GEOTAIL satellite magnetic field measurements are used to examine the 18 April 2002 injection events. The Los Alamos National Laboratories (LANL) 1991-080, 1990-095, 1989-046, and 1994-084 satellites energetic electron and ion flux injection measurements are used to examine the periodic injection events and compare them against the *AL* index. The electron flux plots are for the 50–75 keV, 75–105 keV, 105–150 keV, 150–225 keV, 225–315 keV, 315–500 keV, and 500–750 keV ranges. The energetic proton fluxes are for the 75–113 keV, 113–170 keV, 170–250 keV, 250–400 keV, and 400–670 keV ranges. The ground based measurements for the *AL* and *Dst* geomagnetic indices for the 3–7 October 2000 event were obtained from the World Data Center at Kyoto University. The same data for the 15–24 April 2002 event was obtained from the National Center for Atmospheric Research (NCAR).

[12] The *AL* index is derived from measurement of the horizontal component of the Earth's magnetic field at stations located along the auroral arc in the Northern Hemisphere. It is given for every minute over a 24 hour period in a day and is obtained by selecting the smallest values measured among 12 stations located along the auroral zone, all of them above 50° latitude. The lowest negative values of *AL* are taken to be the strongest activity of the westward auroral electrojet. The *AL* values are a measure of, and compared with, the I_1 current in the WINDMI model. The I_1 current flows horizontally in the lower ionosphere as the closure of the magnetospheric region 1 field-aligned current (R1 FAC) that is generated in the central plasma sheet. This closes the electric current **j** in the nightside magnetosphere through the nightside auroral ionosphere as will be described in section 4. A dimensionless scaling factor is calculated to normalize between the current I_1 and the *AL* index. The method for determining this scaling factor will be described in section 4.1.

[13] The *Dst* indices are obtained from the measurement of the Earth's magnetic field from observatories that are sufficiently distant from the auroral and equatorial electrojets and located at approximately ±20° latitude, while being evenly distributed in longitude. The *Dst* index is compared to the output from the WINDMI model through the ring current energy W_{rc} using the Dessler-Parker-Sckopke relation. WDC Kyoto had both provisional and final indices for use in research but the final indices were only available for storms before 1997. Consequently, both storms for this work were analyzed using the provisional indices.

2.1. Event of 3–7 October 2000

[14] In Figure 1 we show the ACE satellite solar wind and IMF data for 3–7 October 2000. An extended magnetic cloud began at 1018 UT on 3 October and continued until 0534 UT on 5 October [*Wang et al.*, 2003]. The signature of the magnetic cloud can be seen from the plots of B_y^{IMF} and B_z^{IMF} in Figure 1 as sinusoid-like waveforms, the IMF clock angle changes linearly through an angle of 180° through this period. B_z^{IMF} reached minimum values during the sawtooth intervals on 3 October below −13 nT and on 4 October just below −15 nT. Average values in sawtooth intervals are near −10 nT [*Borovsky et al.*, 2007]. Higher-speed solar wind from another disturbance overtaking the magnetic cloud, compressed and enhanced the southward IMF in the trailing edge of the cloud, greatly increasing its geoeffectiveness and leading to a major magnetic storm. The magnetic storm lasted from 3–7 October 2000 but only

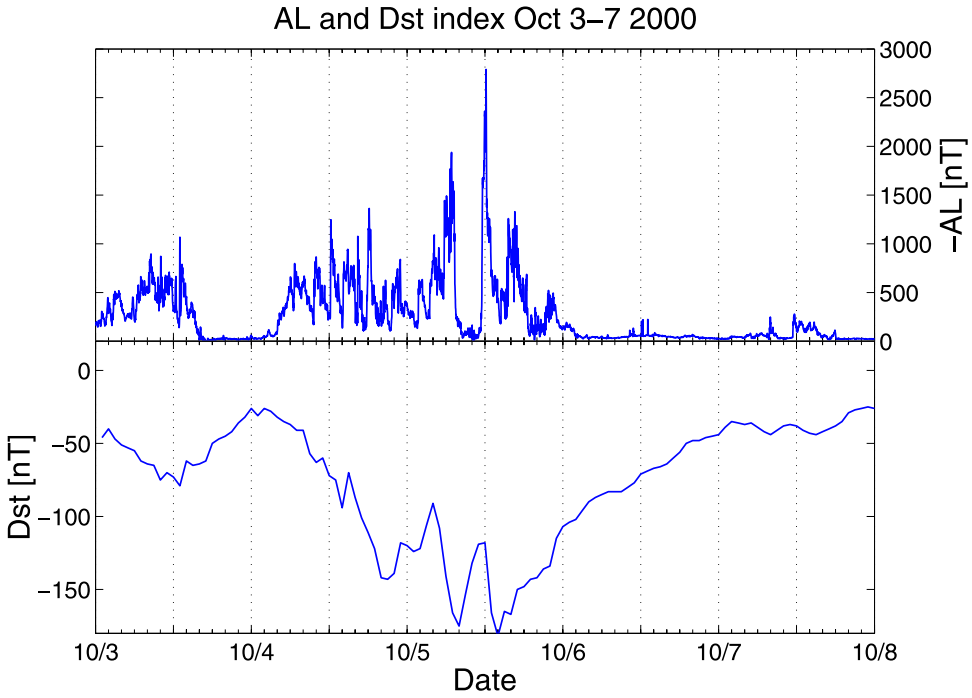

Figure 2. The *AL* and *Dst* indices for 3–7 October 2000. The *AL* index shows two separate periods of sawtooth oscillations, 0800–1600 UT 3 October and 0800–2200 UT 4 October.

reached its most disturbed levels shortly after the trailing edge of the magnetic cloud passed the Earth. The *Dst* reached two minima of −175 nT on 5 October 0800 UT and −182 nT at 1400 UT, as shown in Figure 2. The solar wind data correlates with measurements of the westward auroral *AL* index and the *Dst* index on the same dates.

[15] An interplanetary (IP) shock front propagates past ACE at 0240 UT on 5 October 2000 at a calculated speed of 530 km/s. The first large *AL* spike with a peak of about −1938 nT occurring at 0651 UT 5 October 2000 is triggered by the shock front. A second, larger spike of approximately −2790 nT in the *AL* index occurs at 1210 UT 5 October 2000 initiated by a strong southward IMF excursion detected at ACE about an hour earlier. The *Dst* minimum of −180 nT is reached on 5 October slightly after the strong southward IMF surge.

[16] In this storm, two separate intervals of periodic substorm activity occur: one from about 0800–1600 UT on 3 October 2000 and the other from about 0600–2200 UT on 4 October 2000 during the initial phase of the main storm. The activity in the later interval has been identified as sawtooth oscillations by *Huang et al.* [2003b] and discussed in detail by *Reeves et al.* [2003]. In the earlier interval, there was insufficient local time coverage by the LANL geosynchronous satellites to provide a firm identification of injections as sawtooth events. However, at least one of the injections (onset at ∼1240 UT) appeared to be dispersionless on three satellites at 1400, 1800, and 2000 hours MLT and may be a sawtooth event. Owing to these uncertainties, the auroral activity on 3 October is referred to as an interval of recurrent substorms.

[17] In Figure 3 we show the energetic electron and proton flux data as measured by the LANL satellite 1989–046 to highlight the injection events that occur on 4 October 2000. We observe that the AL index has a sawtooth auroral waveform for every injection event measured by the LANL satellite. The flux maximum is used to identify the sawtooth times and the AL minimum for the correlated substorm times. The injection times shown by the vertical lines in Figure 3 occur at 6.7, 10, 12.25, 14.25, 16.4, 18.2, 20.7, and 22.9 hours.

2.2. Event of 15–24 April 2002

[18] In mid-April 2002, active region (AR) 9906 erupted in three long-duration flare events bathing the Earth in solar energetic particles as it moved across the solar disc. Both the M1.2 class flare on 15 April and the M2.6 class flare on 17 April were associated with full-halo CMEs. The long-duration X1.2 class flare on 21 April produced a partial-halo CME off the Sun's west limb. Shocks were seen by ACE on 17 April, 19 April, and 23 April, signaling the arrival at L1 of solar wind disturbances from these events, as can be seen in Figure 4.

[19] The first shock event occurred during the initial phase of the storm and was observed by ACE at 1020 UT on 17 April with a calculated shock speed of 480 km/s and was followed by a magnetic cloud beginning at approximately 0000 UT 18 April and continuing until 0200 UT 19 April. The origin of the magnetic cloud was a halo CME observed by SOHO/LASCO at 0350 UT on 15 April with a lift-off speed of 720 km/s and a transit time to Earth of ∼55 hours [*Manoharan et al.*, 2004]. B_z^{IMF} fluctuated rapidly in the sheath region dipping below −30 nT at times on 17 April, while in the magnetic cloud, B_z^{IMF} slowly varied over the course of more than 26 hours reaching a minimum value just below −13 nT on 18 April and returning to zero near 0200 UT 19 April (see Figure 4). Again this value is very comparable to the magnetic cloud on 3–4 October 2000 and

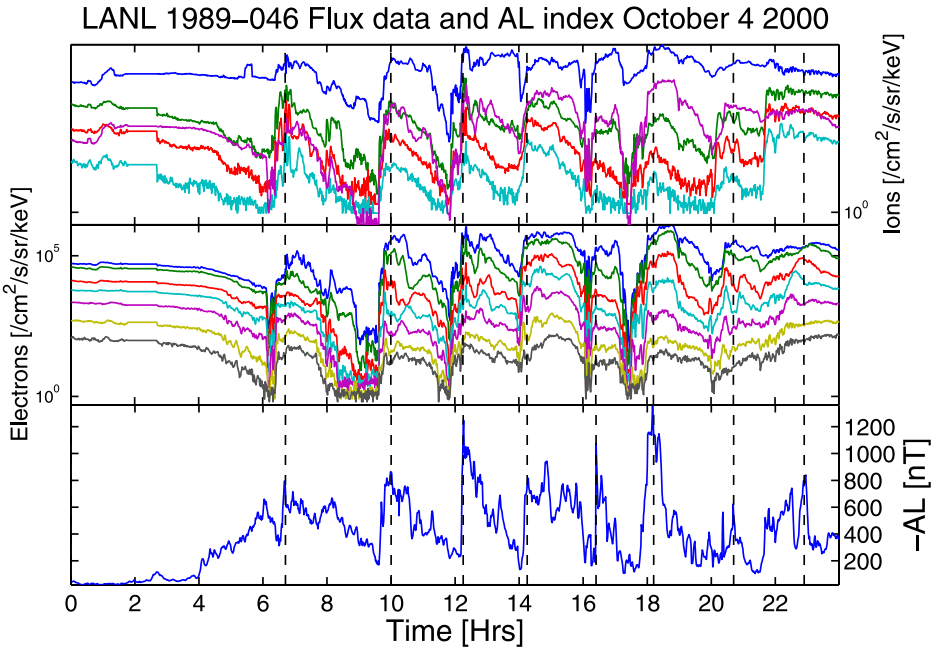

Figure 3. The 4 October 2000 energetic proton and electron flux injection measurements from the LANL 1989-046 spectrometers, compared with the measured geomagnetic *AL* index, showing eight substorm peaks in the *AL* signature directly correlated to the injection events. The LANL flux maximums were used to identify the events.

to B_z^{IMF} sawtooth intervals in general [*Borovsky et al.*, 2007].

[20] The *AL* and *Dst* geomagnetic indices measured between 15 and 24 April are shown in Figure 5. Sawtooth oscillations were observed on 18 April from about 0200 UT to 2100 UT by the GEOTAIL satellite and also by the geosynchronous satellites LANL 1990-095 and LANL 1991-080. This is depicted in Figure 6. The injection times

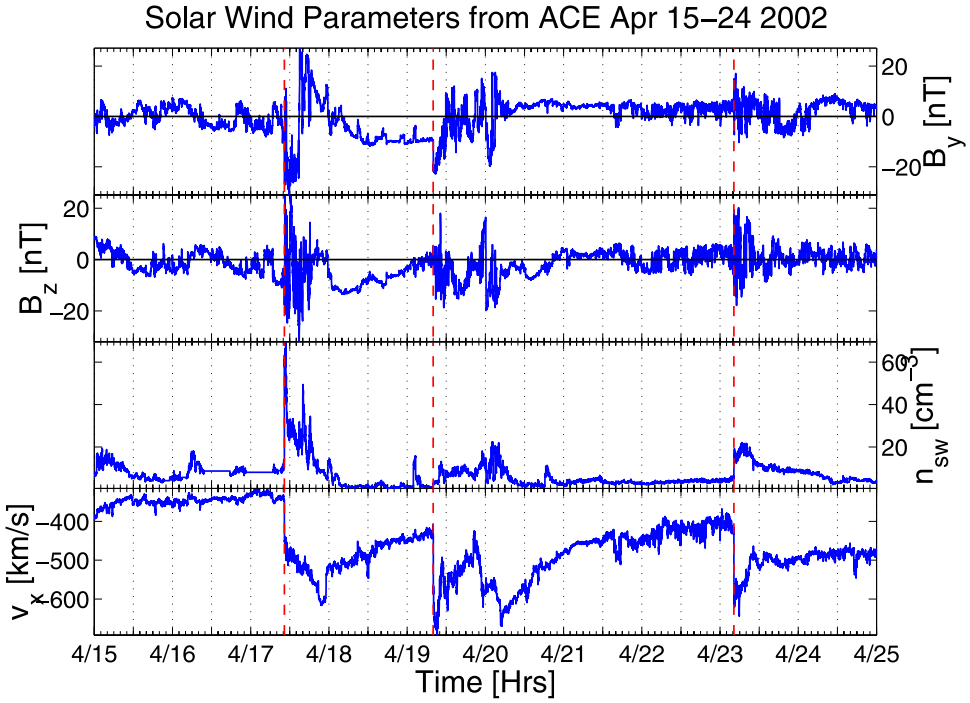

Figure 4. ACE satellite measurements of the solar wind velocity v_x, proton density n_{sw}, and the B_z^{IMF} and B_y^{IMF} component for 15–24 April 2002, in GSM coordinates. The mean position of the satellite during this period was $X = -224, Y = 30, Z = -13$ Earth radii in GSM coordinates. The dashed vertical lines mark the shock events.

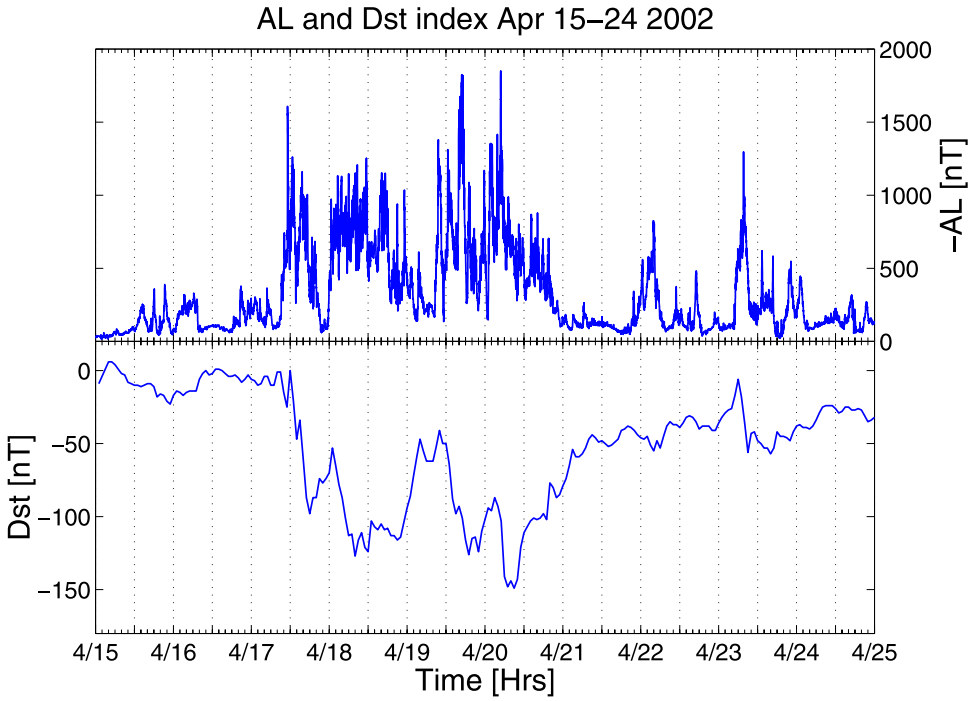

Figure 5. The *AL* and *Dst* indices for 15–24 April 2002. The large spikes in the *AL* signature on 17 April, 19–20 April, and 23 April are initiated by the 3 IP shocks. The main phase of this long geomagnetic storm takes place between 18 and 20 April.

were determined following *Huang et al.* [2003a]. They occur at 0.75, 2.75, 5.58, 8.3, 11.86, 14.32, and 16.62 hours. Much of this interval occurred during relatively steady conditions in the solar wind. This allows one to observe the effects of the sawtooth events on the inner magnetosphere against a background of slowly changing ring current and dynamic pressure signatures, making this one of the clearest examples of sawtooth oscillations to date. Seven oscillations are recorded in the 24 hour period of 18 April, but the satellite observations do not appear to correlate well with *AL* activity. The southward interplanetary magnetic field B_z^{IMF} associated with these two regions produced a double peaked magnetic storm with minima in *Dst* of −98 nT on 17 April and of −127 nT on 18 April, respectively.

[21] The next shock event occurred during the main phase of the storm at 0801 UT on 19 April moving at a calculated shock speed of 650 km/s and is associated with a halo CME leaving the Sun at 0826 on 17 April moving at 1240 km/s [*Cane and Richardson*, 2003]. The associated MC in combination possibly with other interacting ICMEs produced the complex structure observed by ACE from 19 to 21 April. Regions of smoothly rotating B_z^{IMF} reached minimum values of −15 *nT* late on 19 April and −8 nT on 20 April. Though intervals of sawtooth oscillations occurred in this time interval, the signatures were complicated due to the interacting ICMEs. This solar wind disturbance triggered a magnetic storm with four minima in the *Dst*. The first sheath/CME combination in the complex ejecta initiated the magnetic storm on 19 April reaching minimum *Dst* values of −126 nT and −124 nT as the storm was building in the main phase. The storm peak on 20 April was characterized by double minima in *Dst* of −148 nT and −149 nT associated with two peaks in southward B_z^{IMF} in the second shock/sheath region, as observed from Figure 5. The recovery phase was interrupted by a local minimum of −100 nT driven by the relatively weak southward B_z^{IMF} in the second magnetic cloud on the trailing edge of the solar wind disturbance.

[22] The third shock event occurred at 0413 UT on 23 April moving with a calculated shock speed of 690 km/s and is associated with a partial halo CME leaving the Sun at 0127 UT on 21 April at a speed of 2393 km/s off the west limb. Only the shock/sheath region clipped the Earth producing a moderate magnetic storm with minimum *Dst* of −56 nT. The date, time, and speed of the CMEs are taken from the SOHO LASCO CME catalog.

[23] The geoeffectiveness of the three shock events can be seen in the *AL* signature of Figure 5. A large peak of −1600 nT occurs on 17 April at about 1100 UT, initiated by the first shock. The second shock produced two intense peaks of −1824 nT at about 1648 UT 19 April and −1851 nT at approximately 0451 UT 20 April. Finally, the third shock initiates an *AL* surge of −1297 nT at approximately 0741 UT 23 April.

3. Solar Wind Input

[24] The ACE satellite orbits the L1 point about 1.5 million km (approx. 235 Earth radii) from Earth and 148.5 million km from the Sun. The orbit is a modified halo with a major axis A_y of about 2.6×10^5 km and a minor axis A_z of about 1.6×10^5 km (approx. $41.4R_E$ and $24.7R_E$, respectively). The properties of the solar wind are not expected to vary considerably over the satellite's orbit. The solar wind proton density n_{sw}, the solar wind velocity

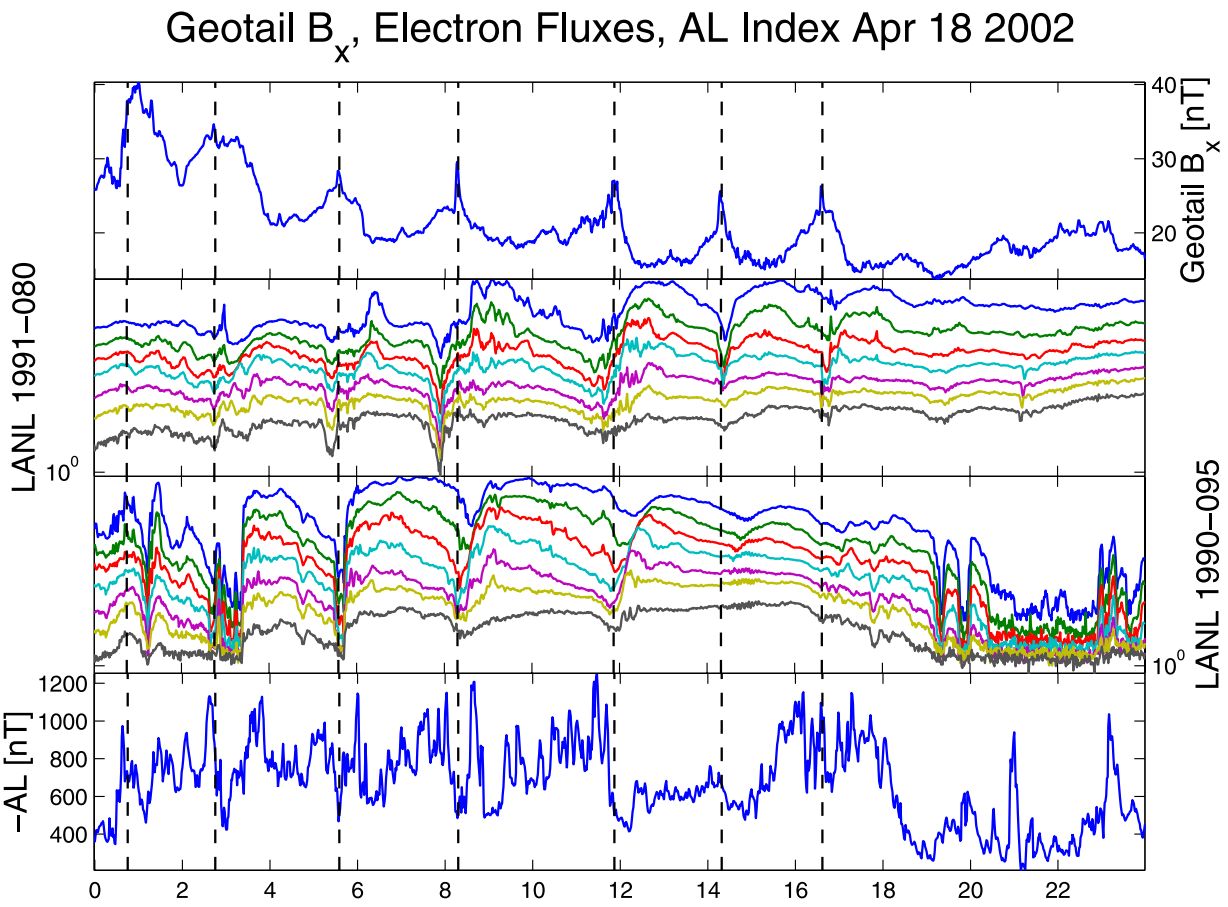

Figure 6. The 18 April 2002 energetic electron fluxes injection measurements, compared with the *AL* index and Geotail magnetic field measurements. Only Geotail B_x measurements are shown here, but the injection peaks appear at the same times in the B_y and B_z measurements. The average Geotail location during this period was (−26, 12, 9) R_E.

v_x, v_y, v_z, the magnetic fields B_x^{IMF}, B_y^{IMF}, B_z^{IMF}, and the location of the satellite X, Y, Z in GSM coordinates are obtained for input into the WINDMI model. The magnetic field values are given every 16 s, while the proton density and solar wind velocity are given every 64 s. Since the data are given with different time stamps, linear interpolation is used to specify the parameters over 60-s intervals. This was done in order that the input data be compatible with the AL index data format, which is specified over 60-s intervals. Missing or unusable data from ACE satellite measurements were dealt with by retaining the previous data value whenever the data was unusable. If unusable data occurred at the first point of the time series, the value was set to zero.

3.1. Time Delay

[25] The position of the ACE satellite introduces a time delay for the solar wind to transit from the L1 point to the nominal coupling region at $X = 10R_E$. This time delay is approximately 1 hour. For this work we use:

$$t(V,X,Y) = \frac{X - X_0}{V} \tag{1}$$

where t is the time delay and $X_0 = 10R_E$ and V is the solar wind bulk speed where we have taken $V = v_x$. This formula implicitly assumes that (1) the solar wind conditions are spatially uniform over the transit distance, (2) the position of the coupling region does not vary with time, and (3) the solar wind discontinuities are parallel to phase fronts. More detailed time delay formulas have been developed by *Weimer et al.* [2003], *Weimer* [2004], and *Bargatze et al.* [2005] but in this work we use the classical formula given by (1). The computed average time delay using the above formula is 53.5 min and 51.5 min for the October 2000 and April 2002 storm periods, respectively. The aberration caused by the Earth's orbital motion at an azimuthal velocity of 29.8 km/s is neglected since in 50 min it amounts to $14R_E$ which is small compared to the radial propagation of the solar wind plasma of approximately $220-230R_E$.

3.2. Input Dynamo Voltage

[26] The driving voltage V_{sw} is calculated in two ways. The first is to use the standard rectified vB_s formula [*Reiff and Luhmann*, 1986], given by

$$V_{sw} = v_{sw} B_s^{IMF} L_y^{eff} \tag{2}$$

where v_{sw} is the x-directed component of the solar wind velocity in GSM coordinates, B_s^{IMF} is the southward IMF

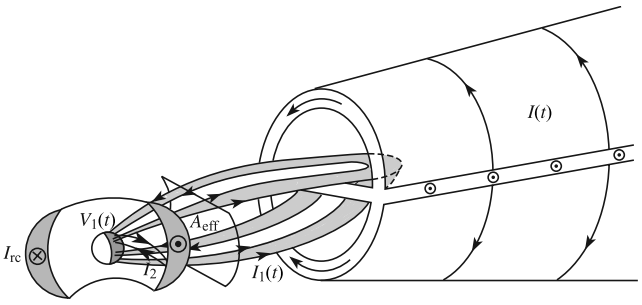

Figure 7. Geometry of the WINDMI model. The energy components V, $K_{||}$, and p in the central plasma sheet are not shown here. A_{eff} is an effective aperture for particle injection into the ring current. I_{rc} is the ring current whose energy is $W_{\rm rc}$ given by equation (12). A second current loop is the $I_1(t)$ R1 FAC current is associated with the westward auroral electrojet and has the associated voltage V_I. The area enclosed by this loop contains a magnetic flux through mutual inductance with the larger geotail cross-field current loop $I(t)$. The field-aligned current at the lower latitude that closes on the partial ring current is designated as I_2.

component and L_y^{eff} is an effective cross-tail width over which the dynamo voltage is produced. For northward or zero B_s^{IMF}, a base voltage of 40 kV is used to drive the system. The second method is to use a model given by *Siscoe et al.* [2002b], *Siscoe et al.* [2002a], and *Ober et al.* [2003] for the coupling of the solar wind to the magnetopause using the solar wind dynamic pressure P_{sw} to determine the standoff distance. This model includes the effects of the east-west component of the IMF and the formula for $V_{sw} = V_{sw}(n_{sw}, \vec{v}_{sw}, \vec{B}^{IMF})$ is given by

$$V_{sw}(kV) = 30.0(kV) + 57.6E_{sw}(mV/m)P_{sw}^{-1/6}(nPa) \qquad (3)$$

where,

$$E_{sw} = v_{sw}\left(\left(B_y^{IMF}\right)^2 + \left(B_z^{IMF}\right)^2\right)^{1/2} \sin\left(\frac{\theta}{2}\right) \qquad (4)$$

is the solar wind electric field with respect to the magnetosphere and the dynamic solar wind pressure $P_{sw} = n_{sw}m_p v_{sw}^2$. Here m_p is the mass of a proton. The IMF clock angle θ is given by $\tan^{-1}(B_y/B_z)$. The solar wind flow velocity v_{sw} is taken to be approximately v_x. The factor $57.6P_{sw}^{-1/6}$ gives the effective length L_y^{eff} of the dynamo region for the complex magnetopause coupling to the magnetosphere. Following *Kivelson and Russell* [1995, pp. 171–172] for the magnetopause stand off distance $(R_{mp}/R_E)^6 = B_{dp}^2/(\mu_0\, P_{sw})$, we find that the effective length over which the dynamo electric field acts to drive the magnetospheric voltage above the base viscous level of 30 kV in (3) is $L_y^{eff} \approx 9R_E/[P_{sw}(nPa)]^{1/6}$. We discuss the differences between the two input voltage in section 4.2.

4. WINDMI Model Description

4.1. Differential Equations of the Model

[27] The plasma physics-based WINDMI model uses the solar wind dynamo voltage V_{sw} generated by either the Siscoe model or the rectified vB_s as the input to drive eight ordinary differential equations describing the transfer of power through the geomagnetic tail, the ionosphere, and the ring current. The WINDMI model is described in some detail in the work of *Doxas et al.* [2004] and *Horton et al.* [2005a]. The model includes ring current energization from substorm injections and gives predicted $D_{\rm st}$ as well as predicted AL as output.

[28] Figure 7 shows the geometry of the model and some of the major energy components. The central plasma sheet energy components are not shown in Figure 7. We also observe from Figure 7 the flux linkage between the southward magnetic field from the plasma sheet current through the area of the region 1 current loop, which creates a mutual inductance between them.

[29] The largest energy reservoirs in the magnetosphere-ionosphere system are the plasma ring current $W_{\rm rc}$ and the geotail lobe magnetic energy W_m formed by the two large solenoidal current flows producing the lobe magnetic fields. These energies are stored as particle kinetic energy in the ring current and a lobe inductance L in the case of W_m. Both W_m and $W_{\rm rc}$ are a few PJ. The value of W_m seldom varies over 10% of its steady state value while $W_{\rm rc}$ is more dynamic, consistent with the Dessler-Parker-Sckopke relation and the observed *Dst* index.

[30] A second current loop is the I_1 R1 FAC current that is associated with the westward auroral electrojet. This current has an associated magnetic energy $\frac{1}{2}\, L_1 I_1^2$, where L_1 is the self-inductance of the region 1 current loop. The area enclosed by the loop contains magnetic flux Φ_{MI} through mutual inductance M with the larger ($\sim$20 times) geotail cross-field current loop I. The field-aligned current at the lower latitude that closes on the partial ring current is designated as I_2. This current is only a part of the total region 2 FAC shielding current system.

[31] Both current loops have associated voltages V and V_I driven by the solar wind dynamo voltage $V_{\rm sw}(t)$. The resultant electric fields give rise to $\mathbf{E} \times \mathbf{B}$ perpendicular plasma flows whose energies are stored in the capacitances C and C_I. There is also parallel kinetic energy $K_{||}$ due to mass flows along the magnetic field lines.

[32] The high-pressure plasma trapped by the reversed lobe magnetic fields gives the thermal energy component $U_p = \frac{3}{2}\, p\Omega_{cps}$, where $\Omega_{cps} = L_x L_y L_z$ is the volume of the central plasma sheet. The partial ring current I_2 transfers energy along magnetic field lines from the ionosphere to the ring current. The ring current is also energized by particle injection across the effective aperture A_{eff} in the transition region [*Doxas et al.*, 2004]. The resulting equations for the state vector $X = (I, V, p, K_{||}, I_1, V_I, I_2, W_{\rm RC})$ in the WINDMI model are given by

$$L\frac{dI}{dt} = V_{\rm sw}(t) - V + M\frac{dI_1}{dt} \qquad (5)$$

$$C\frac{dV}{dt} = I - I_1 - I_{\rm ps} - \Sigma V \qquad (6)$$

$$\frac{3}{2}\frac{dp}{dt} = \frac{\Sigma V^2}{\Omega_{\rm cps}} - u_0 p K_{||}^{1/2}\Theta(u) - \frac{pVA_{\rm eff}}{\Omega_{\rm cps}B_{\rm tr}L_y} - \frac{3p}{2\tau_E} \qquad (7)$$

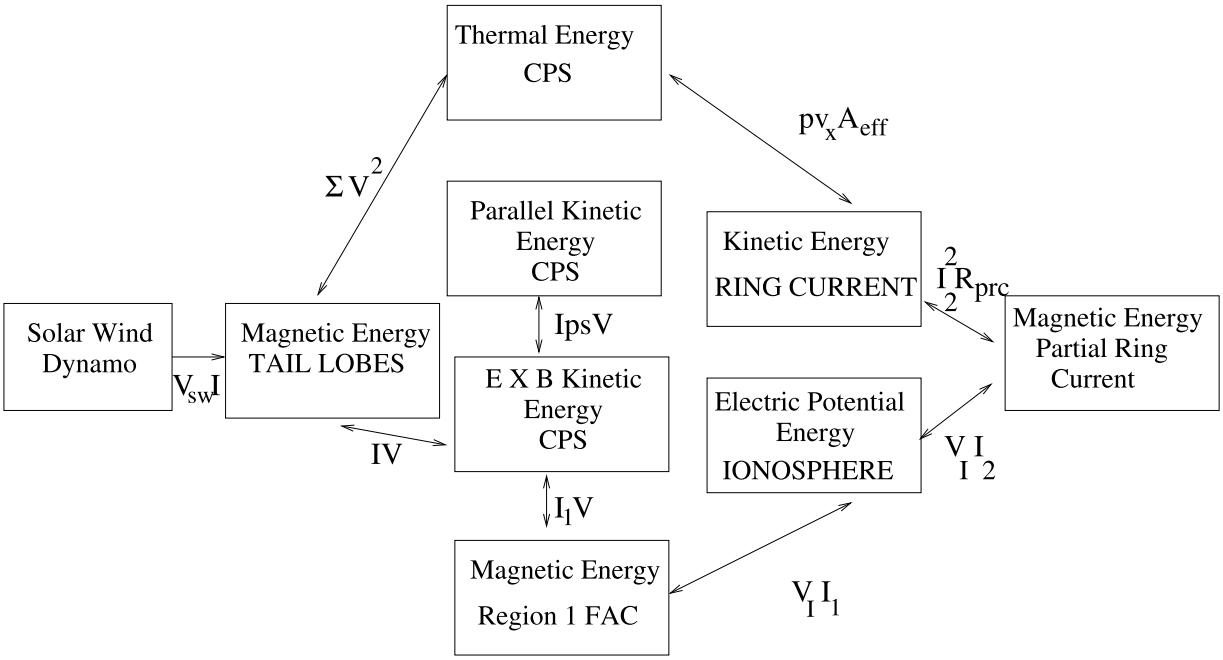

Figure 8. Energy flows in the WINDMI model. The energy transfer from the mutual inductance terms and the energy dissipation paths are not shown here. The average velocity of the particles across the Alfvén layer is given by $v_x = V/(B_{tr}L_y)$.

$$\frac{dK_{||}}{dt} = I_{ps}V - \frac{K_{||}}{\tau_{||}} \tag{8}$$

$$L_I\frac{dI_1}{dt} = V - V_I + M\frac{dI}{dt} \tag{9}$$

$$C_I\frac{dV_I}{dt} = I_1 - I_2 - \Sigma_I V_I \tag{10}$$

$$L_2\frac{dI_2}{dt} = V_I - \left(R_{\rm prc} + R_{A2}\right)I_2 \tag{11}$$

$$\frac{dW_{\rm rc}}{dt} = R_{\rm prc}I_2^2 + \frac{pVA_{\rm eff}}{B_{\rm tr}L_y} - \frac{W_{\rm rc}}{\tau_{\rm rc}} \tag{12}$$

[33] We may obtain an energy equivalent representation of the state space system by multiplying (5) by I, (6) by V, (7) by $\Omega_{\rm cps}$, (9) by I_1, (10) by V_I, and (11) by I_2. Upon doing this, we get nine pairs of energy transfer terms as follows:

[34] 1. The power transfer $-IV$ and IV between equations (5) and (6) which transfers magnetic energy stored in the geotail lobe to $\mathbf{E} \times \mathbf{B}$ earthward plasma flows in the central plasma sheet.

[35] 2. The power transfer $-I_{\rm ps}V$ and $I_{\rm ps}V$ between equations (6) and (8) which converts pressure gradient driven perpendicular kinetic energy to parallel flows by assuming incompressible flow.

[36] 3. The power transfer $-\Sigma V^2$ and ΣV^2 between equations (6) and (7) which converts collisionless ohmic heating to pressure in the central plasma sheet [*Horton and Tajima*, 1991].

[37] 4. The power transfer $-I_1V$ and VI_1 between equations (6) and (9) that results from the cross-tail electric field driving the region 1 FAC.

[38] 5. The power transfer $-V_II_1$ and V_II_1 between equations (9) and (10) which is the conversion between magnetic energy stored in the I_1 current loop and the electrostatic energy stored in the ionospheric capacitance C_I.

[39] 6. The power transfer $-V_II_2$ and V_II_2 between equations (10) and (11) which is the transfer of energy due to the ionospheric voltage V_I driving the partial ring current I_2.

[40] 7. The power transfer $-I_2^2R_{\rm prc}$ and $I_2^2R_{\rm prc}$ between equations (11) and (12), the energization of the ring current through ohmic losses.

[41] 8. The power transfer $\pm pVA_{\rm eff}/(\Omega_{\rm cps}\ B_{\rm tr}\ L_y)$ between equations (7) and (12), which describes the particle injection across the Alfvén layer.

[42] 9. The interaction energy $MIdI_1/dt$ and MI_1dI/dt between equations (5) and (9) arising from the mutual inductance terms.

[43] The transfer of energy between the different global reservoirs is shown in Figure 8.

[44] The nonlinear dynamics of the model traces the flow of the dynamo generated power by electromagnetic and mechanical means through the eight pairs of transfer terms. The remaining terms describe the loss of energy from the magnetosphere-ionosphere system through plasma injection, ionospheric losses, and ring current energy losses. The system of eight ordinary differential equations which make up the model follows the conservation rules of network theory.

Table 1. WINDMI Nominal Parameters, Estimated By Physical Considerations of the State and Geometry of the Nightside Magnetosphere Using the Tsyganenko Magnetic Field Model[a]

Parameter	Value	Description
L	90 H	Inductance of the lobe cavity surrounded by the geotail current $I(t)$. The nominal value is $L = \mu_0 A_\ell / L_x^{\text{eff}}$ in Henries where A_ℓ is the lobe area and L_x^{eff} the effective length of the geotail solenoid. Computation of L as function of the IMF from the Tsyganenko model are given by *Horton and Pekker* [1998].
M	1 H	The mutual inductance between the nightside region 1 current loop I_1 and the geotail current loop I.
C	50000 F	Capacitance of the central plasma sheet in Farads. The nominal value is $C = \rho_m L_x L_z/(B^2 L_y)$ where ρ_m is the mass density in kg/m^3, $L_x L_z$ is the meridional area of the plasma sheet, L_y the dawn-to-dusk width of the central plasma sheet and B the magnetic field on the equatorial plane. Computations of C are given by *Horton and Doxas* [1996].
Σ	8 S	Large gyroradius ρ_i plasma sheet conductance from the quasineutral layer of height $(L_z\rho_i)^{1/2}$ about the equatorial sheet. The nominal value is $\Sigma = 0.1\ (n_e/B_n)(\rho_i/L_z)^{1/2}$. Computation of Σ is given by *Horton and Tajima* [1991].
Ω_{cps}	2.6×10^{24} m^3	Volume of the central plasma sheet that supports mean pressure $p(t)$, initial estimate is $10^4 R_E{}^3$.
u_0	4×10^{-9} m^{-1} kg$^{-1/2}$	Heat flux limit parameter for parallel thermal flux on open magnetic field lines $q_{\|\|} = const \times v_{\|\|} p = u_0 (K_{\|\|})^{1/2} p$. The mean parallel flow velocity is $(K_{\|\|}/(\rho_m\, \Omega_{cps}))^{1/2}$.
I_c	1.78×10^7 A	The critical current above which unloading occurs.
α	8×10^{11}	The geotail current driven by the plasma pressure p confined in the central plasma sheet. Pressure balance between the lobe and the central plasma sheet gives $B_\ell^2/2\mu_0 = p$ with $2L_x B_\ell = \mu_0 I_{ps}$. This defines the coefficient α in $I_{ps} = \alpha\, p^{1/2}$ to be approximately $\alpha = 2.8\, L_x/\mu_0{}^{1/2}$.

[a]See Table 2 for other parameters.

[45] In the differential equations the coefficients are physical parameters of the magnetosphere-ionosphere system. The quantities L, C, Σ, L_1, C_I, and Σ_I are the magnetospheric and ionospheric inductances, capacitances, and conductances, respectively. A_{eff} is an effective aperture for particle injection into the ring current. The resistances in the partial ring current and region-2 current I_2 regions are R_{prc} and R_{A2}, respectively, and L_2 is the inductance of the region-2 current. The coefficient u_0 in (7) is a heat flux limiting parameter.

[46] The confinement times for the central plasma sheet, parallel kinetic energy, and ring current are τ_E, $\tau_{||}$, and τ_{rc}. The effective width of the magnetosphere is L_y and the transition region magnetic field is given by B_{tr}. The pressure gradient driven current is given by $I_{ps} = L_x(p/\mu_0)^{1/2}$, where L_x is the effective length of the magnetotail.

[47] The pressure unloading function $\Theta(u) = \frac{1}{2}[1+ \tanh u]$ where $u = (I - I_c)/\Delta I$ in equation (7) is specified by a critical current I_c and the interval ΔI for the transition to loss of plasma along newly opened magnetic field lines with a parallel thermal flux $q_{||}$. It changes from zero to unity as a function of I compared to I_c. The unloading function follows from current gradient driven tearing modes or cross-field current instabilities, as described by *Yoon et al.* [2002].

[48] The parameters are combined appropriately into a vector $\mathbf{P}^{\text{d}}$ where $d = 18$. They can be estimated using semianalytical techniques or they can be considered as variables that need to be optimized within physically allowable ranges to fit the data for a given storm. Here we approximated the parameters analytically using the Tsyganenko magnetic field model and then defined a range of allowable values over which each parameter is allowed to vary. In Tables 1 and 2 we give the calculated estimates and a short description of the major parameters in the WINDMI model. The calculations are detailed by *Horton and Doxas* [1996], *Horton and Doxas* [1998], and *Doxas et al.* [2004]. Some parameters listed in Tables 1 and 2 occur only as combinations, such as the effective aperture A_{eff}, transitional region magnetic field B_{tr}, and the dawn-to-dusk width of the magnetosphere L_y.

[49] Numerical solution of the eight differential equations gives the state vector $X(t)$ and the associated eight energy components. The Auroral AL index now follows as a magnetic field perturbation ΔB_{AL} from the ambient terrestrial field due to the westward electrojet current that flows in the E-layer ($\sim$90–120 km) in the nightside ionosphere. The current I_1 used in the model is that portion of the field-aligned region 1 current that maps to the nightside central plasma sheet and is considered to be part of the substorm current wedge that produces the westward auroral electrojet.

[50] We take the westward auroral electrojet index to be proportional to the region 1 current because that current

Table 2. WINDMI Nominal Parameters, Estimated By Physical Considerations of the State and Geometry of the Nightside Magnetosphere Using the Tsyganenko Magnetic Field Model[a]

Parameter	Value	Description
$\tau_{\|\|}$	10 min	Confinement time for the parallel flow kinetic energy $K_{\|\|}$ in the central plasma sheet.
τ_E	30 min	Characteristic time of thermal energy loss through earthward and tailward boundary of plasma sheet.
L_1	20 H	The self-inductance of the wedge current or the nightside region 1 current loop $I_1(t)$
C_I	800 F	The capacitance of the nightside region 1 plasma current loop.
Σ_I	3 mho	The ionospheric Pedersen conductance of the westward electrojet current closing the I_1 current loop in the auroral (altitude $\sim$100 km, 68°) zone ionosphere.
R_{prc}	0.1 ohm	The resistance of the partial ring current.
τ_{rc}	12 hours	The decay time for the ring current energy.
L_2	8 H	The inductance of the region 2 current.
R_{A2}	0.3 ohm	Resistance of the region 2 footprint in the Auroral Region.
B_{tr}	5×10^{-9} T	The magnetic field in the transition region.
A_{eff}	8.14×10^{13} m^2	The average effective area presented to the geotail plasma for plasma entry into the inner magnetosphere, estimated to be $2R_E{}^2$.
L_y	3.2×10^7 m	The effective width of the Alfven layer aperture, estimated to be $5R_E$.
ΔI	1.25×10^5 A	The rate of turn-on of the unloading function.

[a]See Table 1 for other parameters.

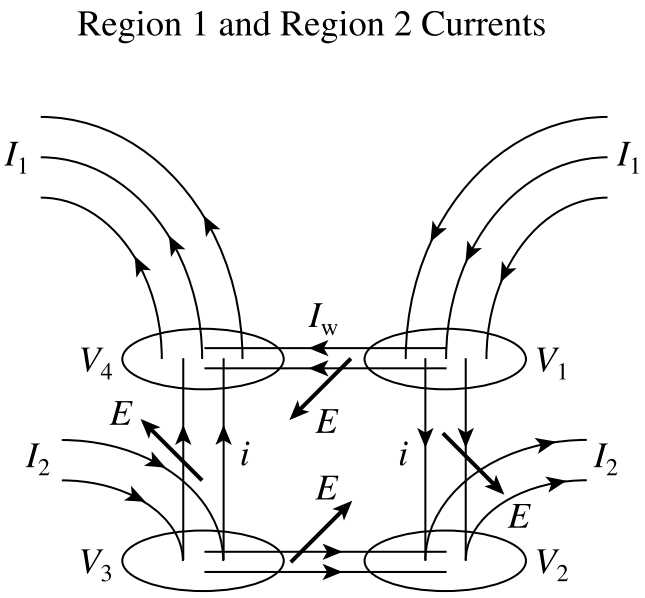

Figure 9. Geometry of the region 1 and region 2 current loop closing in the ionosphere. I_1 is taken to be proportional to the westward auroral electrojet. I_2 is the partial ring current. The southward electric field drives a Hall current westward contributing strongly to the westward electrojet. V_1 to V_4 are the potentials at each footpoint.

loop dominates the aurora current loop shown in Figure 9. The region has a rectangular pattern with four nodes defined by four footpoints of the region 1 and 2 nightside field-aligned currents. The current voltage relations are determined by the Hall and Pederson conductivities giving the southward component of the tilted electric fields in response to the auroral current path. We have worked out the circuit equations for the internal loop current i that links I_1 and I_2. The formulas and their application support the conclusion that the AL index can be taken as directly proportional to the I_1 current.

[51] We estimate the relation between I_1 and the AL index by assuming for simplicity that the current I_1 is related linearly to the AL index by a constant of proportionality $\lambda_{AL}[A/nT]$, giving $\Delta B_{AL} = -I_1/\lambda_{AL}$. The physics estimate of λ_{AL} from a strip approximation of the current I_1 gives a fixed scale between the current I_1 and the AL index. However, an optimized linear scale yields better results of λ_{AL} than the fixed scale which does not take into changes in width, height, and location during geomagnetic activity.

[52] To obtain better values of λ_{AL}, we used estimated physical parameters from Tables 1 and 2 to run the WINDMI model for each of the storms with the Siscoe and rectified drivers separately to obtain the ratio between the mean of the AL index and the mean of I_1. This average value of λ_{AL} for each storm was then used in all subsequent analysis. The scaling factor for the 3–7 October 2000 storm was calculated to be 3275, while for the 15–24 April 2002 storm it was computed to be 2638, both in A/nT.

[53] The D_{st} signal is given by ring current energy W_{rc} (usually in the range $\sim 3-8 \times 10^{15}$ J) through the Dessler-Parker-Sckopke relation:

$$D_{st} = -\frac{\mu_0}{2\pi}\frac{W_{rc}(t)}{B_E R_E^3} \tag{13}$$

where W_{rc} is the plasma energy stored in the ring current and B_E is the Earth's surface magnetic field along the equator. For $W_{rc} = 3 \times 10^{15}$J we get $D_{st} = -74.5$ nT. Tail current effects which can produce up to a 20% increase in the *Dst* have not been included in our model [*Turner et al.*, 2000; *Ohtani et al.*, 2001].

4.2. WINDMI Output With Nominal Parameters

[54] In this work the Average Relative Variance (ARV) is used as a measure of performance for the goodness of fit between the WINDMI model output and the measured AL and *Dst* indices. The ARV is given by

$$ARV = \frac{\Sigma_i (x_i - y_i)^2}{\Sigma_i (\bar{y} - y_i)^2} \tag{14}$$

where x_i are model values and y_i are the data values. In order that the model output and the measured data are closely matched, ARV should be closer to zero. The performance measure is calculated using the model output I_1 or *Dst* as x versus the measured AL or *Dst* index as y. For the ARV measure being less than unity we speak of $(1 - ARV) \times 100\%$ of the variation of the data being explained by the model. A model giving $ARV = 1$ is equivalent to using the average of the data for the prediction. $ARV = 0$ when every $x_i = y_i$.

[55] The Siscoe voltage driver model was consistently found not to produce peak voltages that are as high as the voltages produced by the rectified vB_s formula. Also, the Siscoe model saturates smoothly to the base viscous level while the rectified vB_s drops abruptly to the base voltage when B_z^{IMF} goes positive. This difference is most noticeable during the passage of magnetic clouds in the October 2000 and April 2002 storms when the IMF rotates for a period in the $y-z$ plane. The Siscoe driver produces a smoothly varying input as the clock angle rotates, while the rectified driver cuts off when the clock angle exceeds 90°.

[56] The difference between the two input voltages can be seen in the top of Figures 10 and 11 for the 3–7 October 2000 storm. When using the rectified driver, the activity on 4 October begins at about 0400 UT, whereas the Siscoe driver shows slowly increasing activity beginning at 2200 UT on 3 October and continuing through 4 October, during the rotation of the IMF clock angle within the magnetic cloud. On 5 October the differences are most notable in the peak voltages produced by either driver. While the timing of the peaks are roughly equal, the rectified voltage produces peaks corresponding to the shock events that are close to 1000 kV while the Siscoe driver yields voltages in the 600–700 kV range for the same events. We also observe that there is a period on 5 October between 0730 UT and 1100 UT where the rectified driver shows negligible activity while the B_z^{IMF} is northward. In contrast, the Siscoe driver produces voltages above the base level during this time because B_y^{IMF} is appreciable.

[57] Similar differences were observed with the two drivers for the April 2002 storm. Comparison of the tops of Figures 12 and 13 show that the rectified driver produces peak voltages in excess of 1000 kV while the Siscoe driver does not exceed 750 kV during the three shock events of 17, 19, and 23 April. During the passage of the magnetic cloud on 18 April, the rectified input has the same character as in the October 2000 storm, showing an abrupt increase in

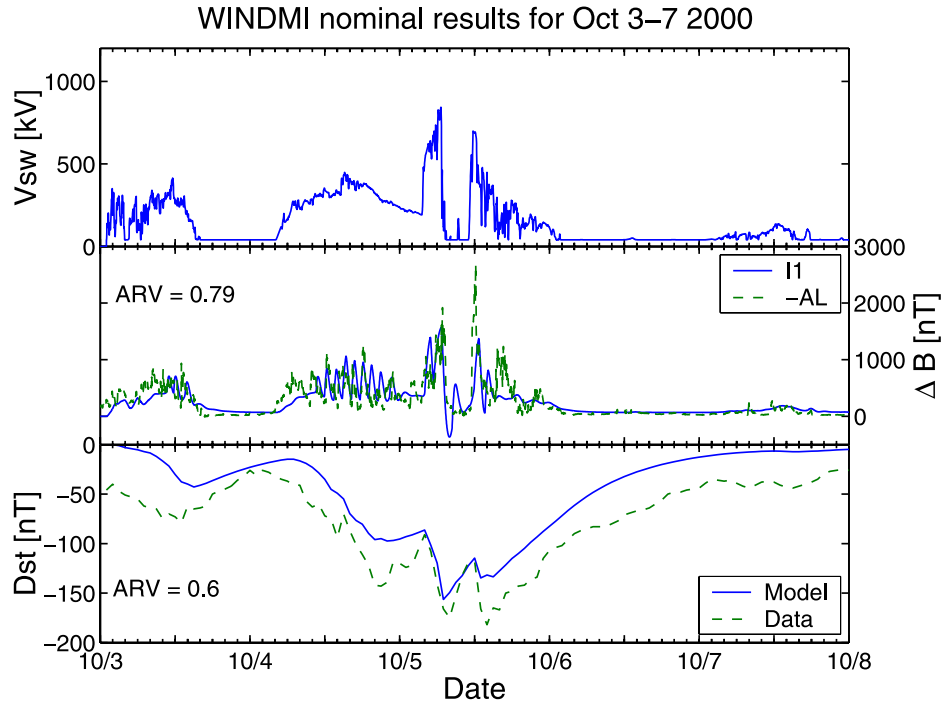

Figure 10. The 3–7 October 2000 WINDMI output using nominal parameters with the rectified vB_s input voltage. The *AL* ARV is calculated for 4 and 5 October. The *Dst* ARV is calculated for 3–7 October. The rectified driver does better with the *Dst* prediction, giving ARV = 0.6 compared to ARV = 0.97 with the Siscoe driver in Figure 11.

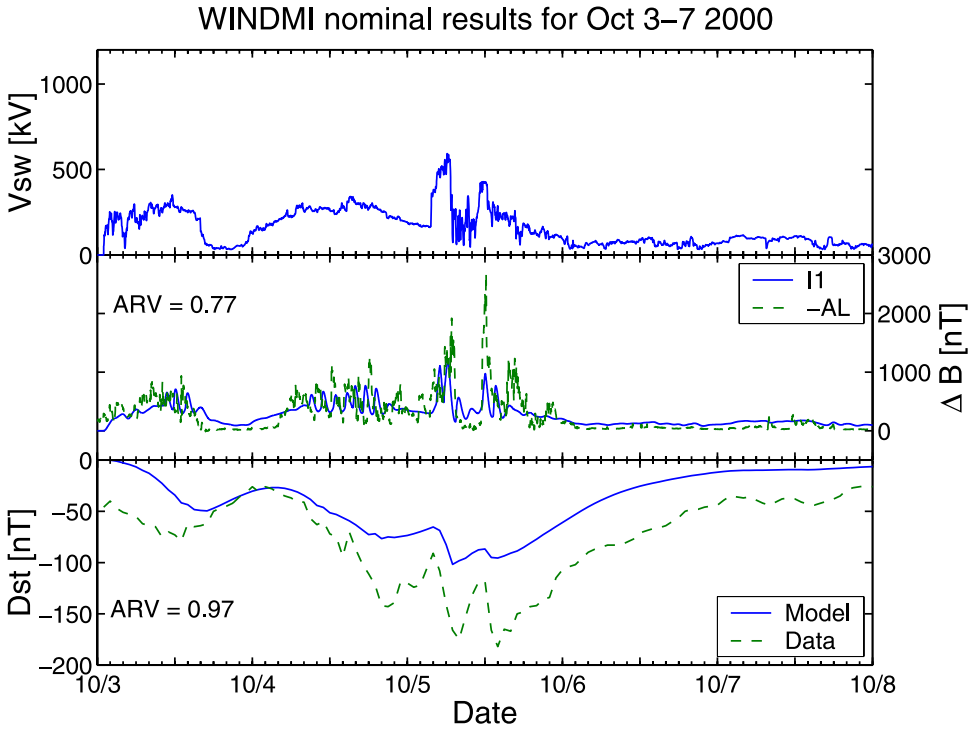

Figure 11. The 3–7 October 2000 WINDMI output using nominal parameters with the Siscoe input voltage. The *AL* prediction with the Siscoe driver with nominal parameters gives an *ARV* = 0.77 which is similar to *ARV* = 0.79 with the rectified driver in Figure 10.

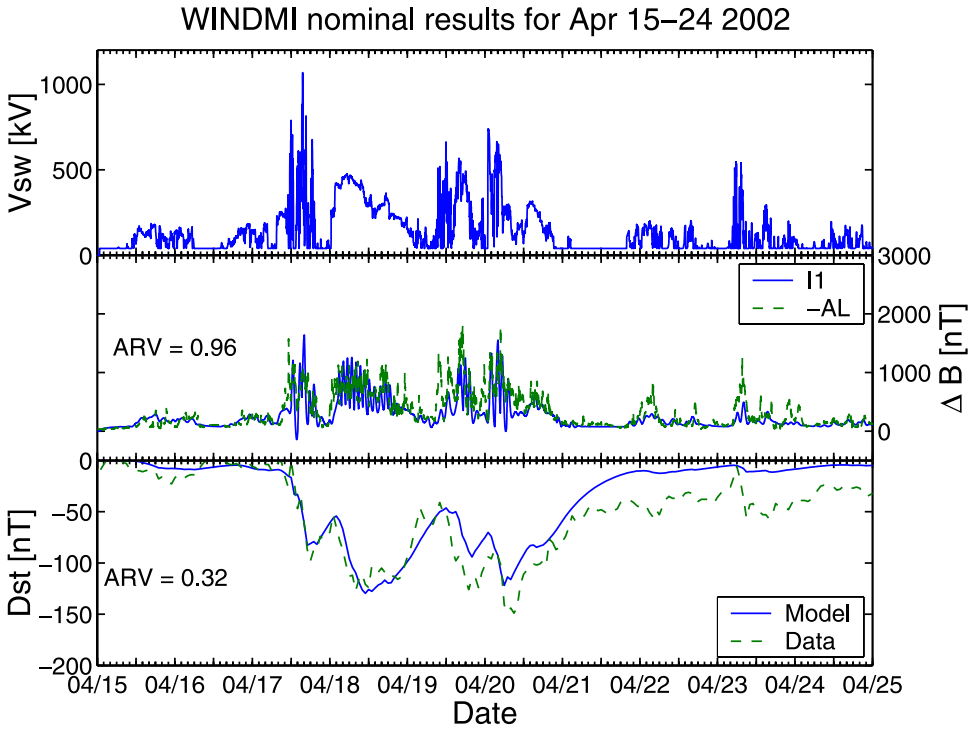

Figure 12. The 15–24 April 2002 WINDMI output using nominal parameters with the rectified input voltage. The *AL* ARV is calculated for 17–20 April. The *Dst* ARV is calculated for 15–24 April. The rectified driver with nominal parameters gives the lowest ARV for the *Dst* as well as *AL* prediction for this storm.

activity at about 0030 UT 18 April and decreases to very low levels between 0100 UT and 0900 UT on 19 April. Similar to the earlier storm, the Siscoe voltage increases gradually beginning more than 2 hours earlier, from 2200 UT 17 April, and sustains moderate activity due largely to IMF B_y into the second shock event of 19 April.

[58] The output of the WINDMI model for the 3–7 October 2000 storm using the nominal calculated esti-

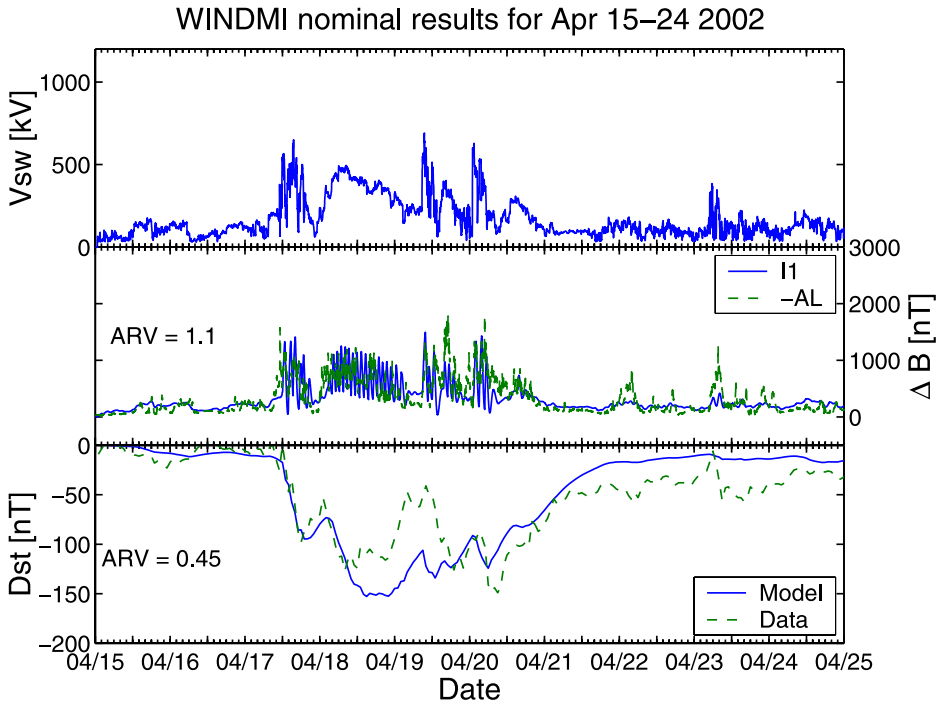

Figure 13. The 15–24 April 2002 WINDMI output using nominal parameters with the Siscoe input voltage. The Siscoe driver with nominal parameters gives a poor *AL* ARV ($\geq$1) for this storm.

mates of parameters from Tables 1 and 2 with the rectified input is shown in Figure 10 and with the Siscoe input is shown in Figure 11. The middle shows the predicted *AL* as a solid curve and the *AL* index as a dotted curve. The bottom shows the *Dst* prediction as a solid curve and the *Dst* index as a dotted curve. The nominal model predicts the *Dst* index better with the rectified vB_s driver ($ARV = 0.6$) than the Siscoe driver ($ARV = 0.97$). However, the *ARV* for the *AL* prediction with the Siscoe driver of $ARV = 0.77$ is very nearly equal to $ARV = 0.79$ with the rectified driver. Substorms are triggered for both drivers during the 4 October interval, but the number and period of the oscillations are incorrect with the nominal parameters.

[59] The performance of the model using the nominal parameters on the 15–24 April 2002 storm is slightly different. We observe from the middle and bottom of Figures 12 and 13 that not only does the rectified driver still yield better *Dst* prediction just as in the October 2000 storm, it also does marginally better with the *AL* prediction. The substorms appear on 18 April, but they recur too frequently and the period of each oscillation is too short with the nominal parameters.

5. Optimization With Multiobjective Genetic Algorithm

[60] With the nominal set of parameters, the WINDMI model predicts quite well the overall variations of both the *AL* and *Dst* indices, but it is reasonable that the model would perhaps fare better if the parameters were more representative of the unique state of the magnetosphere during the storm interval of interest. With a correctly optimized set of parameters, the model could be expected to capture features of interest in a storm, such as the sawtooth oscillations, both in period and number.

[61] A genetic algorithm multiobjective optimization scheme was therefore used to select a parameter set for which the output current I_1 from WINDMI most closely matches the *AL* index and also displays the periodic substorm activity over the relevant interval within a storm. The optimized model was also simultaneously expected to predict the *Dst* index as accurately as possible.

[62] Genetic algorithms are general search and optimization methods that are inspired by the concepts of crossover, random mutation, and natural selection from evolutionary biology. In the current context, one form of the genetic algorithm [*Coley*, 2003] is applied to search the physical parameter space in order to minimize the error between the model output and the measured geomagnetic indices, while attempting to extract solutions with substorm-like features. In earlier works with simpler models, the alternate-gradient, steepest-descent, and simulated annealing methods were used to find optimal parameters. These methods were found to have problems that do not seem to affect genetic algorithms. Stochastic search methods such as genetic algorithms are known to perform better in search spaces where objective functions have multiple local minima and are consequently suitable for complex state-space systems such as the WINDMI model.

[63] The method of selecting parameters depends on the minimization of single or multiple objective functions. In a single objective optimization problem, a single objective or cost function is minimized through the genetic algorithm scheme, and a unique solution set of parameters is obtained. However, it is more usual for a problem to have multiple criteria of varying importance to be met. For instance, in the present case, we need to select parameters so as to simultaneously have good *AL* as well as *Dst*. There may be a trade off in selecting the best solution. We have found through experimentation that in some instances better *Dst* performance needed to be sacrificed to obtain a good *AL* prediction, and vice versa.

[64] A common approach to simultaneously satisfy multiple criteria given by multiple objective functions f_k is by assigning weighting coefficients w_k to each f_k and optimizing against a composite objective function, $F = \sum_k w_k f_k$, with the w_k normalized such that $\sum_k w_k = 1$. This procedure is essentially a variant of the single-objective optimization problem. The weakness of this method is that the weighting coefficients are difficult to systematically assign, and usually the relative weightings are decided by trial and error.

[65] Multiobjective optimization [*Deb*, 2001] is more often applicable when possibly conflicting objectives are to be met in an optimization routine or, as in the present case, qualitative features of a solution needs to be retained even if the main objective criteria is not met. Genetic algorithms are naturally suitable for multiobjective optimization problems because they can be easily modified to retain multiple solutions while searching the parameter space. Multiobjective algorithms apply a simple mathematical rule called domination to update the family of solutions that is carried forward from generation to generation. A multiobjective optimization scheme returns a family of solutions that emphasize the importance of different objective functions in an implicit manner.

[66] The final family of solutions can then be examined, and the best solution that fits the subjective requirements of the problem can be selected. The final selection of a solution is performed by the user usually by using a qualitative criteria rather than a quantitative one. It is important that the optimization scheme simultaneously returns a variety of optimal solutions in order that all combinations of relative importance between the different objective functions are fully explored. This requirement makes the genetic algorithm procedure particularly suitable to multiobjective optimization, since the search space is explored in a random, distributed sense.

[67] The selection of appropriate cost functions or fitness metrics is critical since the features of an optimized solution depends on the cost function. The usual cost functions are the least squares fit or least mean squares fit measures between the model and data time series. In addition to these, we explored a number of different cost functions to investigate the quality of solutions returned by the algorithm.

[68] Among the cost functions explored were as follows:

[69] 1. A normalized l^2 norm (least squares fit) for either *AL* or *Dst*, used in place of the ARV during optimization. The formula for the l^2 norm is

$$||Y||_{l^2} = \frac{1}{\max |y_i|}\left[\Sigma_i (x_i - y_i)^2\right]^{1/2} \tag{15}$$

where x_i are model values and y_i are the data values.

Table 3. Storm Key Optimized Parameters for 3–7 October 2000 Obtained Through Genetic Algorithm Optimization

Parameter	GA Rectified	GA Siscoe
L, H	76	55
C, F	140,000	84,000
Σ, mho	10	7.8
u_0	5.8×10^{-9}	2.5×10^{-9}
I_c, A	1.4×10^{7}	2.6×10^{7}
Σ_I, mho	1.8	2.5
τ_{rc}, s	54,000	30,000
A_{eff}, m^2	4.8×10^{13}	4.3×10^{13}

[70] 2. A normalized l^p norm, $p > 2$, used to emphasize regions of maximum discrepancy between the data and the model, where p is even. We also used the resulting cost function in the limit $p \rightarrow \infty$, which is the maximum norm. The formula for the normalized l^p and l^∞ norms are

$$||Y||_{l^p} = \frac{1}{\max |y_i|} [\Sigma_i (x_i - y_i)^p]^{1/p} \tag{16}$$

$$||Y||_{l^\infty} = \frac{\max |x_i - y_i|}{\max |y_i|} \tag{17}$$

[71] 3. The correlation coefficient, given by

$$COR = \frac{\Sigma_i (x_i - \bar{x})(y_i - \bar{y})}{\sigma_x \sigma_y} \tag{18}$$

[72] 4. The ARV, given in (14).

[73] 5. The number of of oscillations that we define as N_{osc}^{AL} with period 2–3 hours in the *AL* model output signature. This cost function is not given by a formula; rather it is implemented as a signal processing algorithm applied to the output time series. It is used only in conjunction with one of the other norms and a balance of importance between them chosen during the selection process.

[74] Further details of the implementation of the single and multiobjective optimization method for the selection of parameter sets for the two storms analyzed here will be given in Appendix A. For the results presented here, we selected and optimized against three objective functions simultaneously, the least squares fit for the *AL* given by $||AL||_{l2}$, the least squares fit for the *Dst* given by $||Dst||_{l2}$, and N_{osc}^{AL}.

[75] The resolution used for the optimization process was 5 bits, thus each parameter could take 32 possible values. The search space then has $32^{18} = 1.2379 \times 10^{27}$ distinct solutions. A dense search for the optimal solution would be prohibitively long, since each solution with a given set of parameters takes about a second to simulate. After some experimentation, it was found that running the multiobjective genetic algorithm optimization scheme returned a stable family of solutions after searching for about 1000 generations. The period of optimization for the 3–7 October 2000 storm was selected to be between 0000 UT 4 October and 2359 UT 5 October. For the 15–24 April 2002 storm, the optimization period was chosen to be between 000 UT 17 April and 2359 UT 20 April. These intervals were considered to be the most active for each storm during which the state of the magnetosphere should be determined. The ARV measure for the *AL* predictions are calculated during these active periods, but the ARV measure for the *Dst* prediction is calculated over the entire storm period.

[76] The measure of the performance of the model is rather limited in this work due to the fact that we are reporting the ARV and the correlation coeffecients for the same data set used to derive the optimized values. We are evaluating the model with a beta test version using real-time ACE input data and comparing the output results to Quicklook AL and Dst [*Horton et al.*, 2007].

[77] All parameter values were allowed to vary within ±50% of their nominal values, except the central plasma sheet capacitance C. It was found that in order to obtain the sawtooth oscillations, the center value for C needed to be raised to 10^5F and given ±50% variation around this center value. This is up to 10 times greater than the center values we estimated from the density of hydrogen $n_H = 1$ cm^{-3}. This high capacitance value is reasonable if the central plasma sheet during storm times has a high oxygen content. If the oxygen composition of the central plasma sheet is allowed to be from 50% (to 70%) singly ionized atomic oxygen, then we get an increased capacitance C^{O+} over that of hydrogen C^{H+} of $C^{O+}/C^{H+} = 16\, n_O^+/n_H^+ \sim 8 - 10$ which is sufficient to account for the increase given by the GA optimization.

[78] The parameters obtained from the optimization of the model against the two GEM storms are well within the theoretically accepted ranges. Some of these parameter ranges can be estimated by spacecraft data. For example, Cluster gives measures the local thinning of the current sheet down to a thickness of $L_z \sim 900$ km $\leq c/\omega_{pi}$ at densities of order 0.1/cc. The width of the plasma sheet $10R_E \lesssim L_y \lesssim 20R_E$, and the length $50R_E \lesssim L_x \lesssim 100R_E$ also seem within the theoretical expected range based on the magnetopause stand-off distance R_{mp} measured by spacecraft. We may also use the GA values to infer theoretically predicted global average quantities. For example, the GA central plasma sheet capacitance C_{GA} would imply a spatially averaged value of CPS density. Thus, the inferred mean CPS density is given by $\langle \rho \rangle_{GA} \approx B_X' B_n C_{GA} (L_y/L_x)$, where the aspect ratio (L_y/L_x) may not vary much.

6. Optimization Results

6.1. Event of 3–7 October 2000

[79] The optimized results for the 3–7 October 2000 storm using the two different input driver voltages are obtained through examination of the family of results returned by the computational algorithm. The optimized parameters are given in Table 3 and the predicted *AL* and *Dst* results are shown in Figures 14 and 15. The predicted *AL* activity during the sawteeth oscillation period on 4 October is shown in Figures 16 and 17. We see that when using the rectified driver, the *Dst* curves fit very well with the data. In comparison, the Siscoe driver optimized solution does better with the *AL* prediction, returning ARV = 0.65 in contrast to ARV = 0.77 from the optimized rectified driver *AL* prediction.

[80] For either driver, the ARV figures for both the *AL* and *Dst* improve with optimization, as expected. We observe that the *Dst* prediction with the optimized values

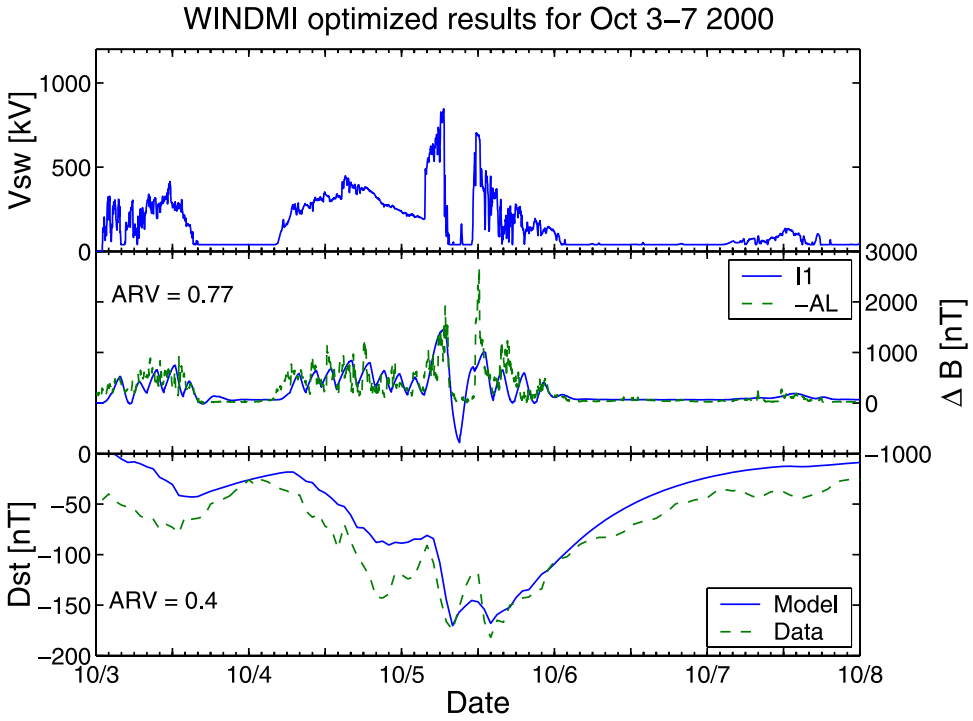

Figure 14. The 3–7 October 2000 optimized using the rectified input voltage. *Dst* prediction improves with ARV = 0.4 compared to ARV = 0.6 with nominal parameters. The overall *AL* only shows slight improvement, but the sawtooth activity on 4 October is better represented than with the nominal parameters, as can be seen in Figure 16.

using the Siscoe driver during the main phase of the storm between 4 October 2100 UT to 5 October 1400 UT is within 20–50 nT of the data, whereas with nominal parameters it underestimates the *Dst* by 60–80 nT. For the nominal as well as the optimized parameter sets, during the early part of the initial phase of this storm between 0000 and 1700 UT 3 October, both drivers underestimate the *Dst* by about 30–40 nT. In the period 1700 UT 3 October to

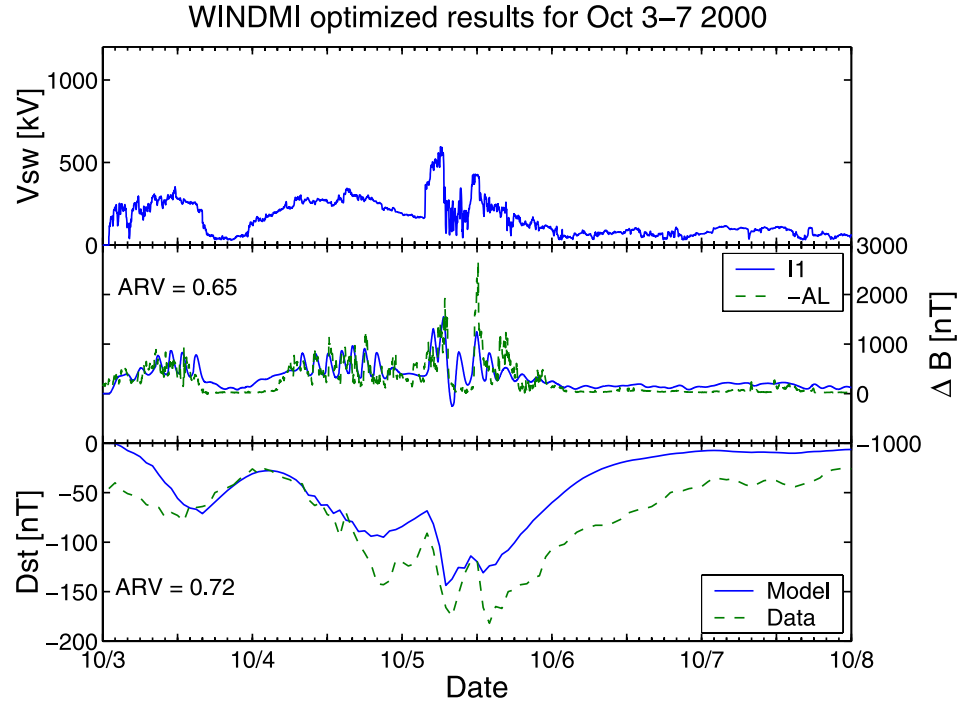

Figure 15. The 3–7 October 2000 optimized using the Siscoe input voltage. Both the the *AL* and *Dst* prediction have improved compared with the nominal model prediction. The sawtooth activity on 4 October is also predicted better here than with the nominal parameters, as shown in Figure 17.

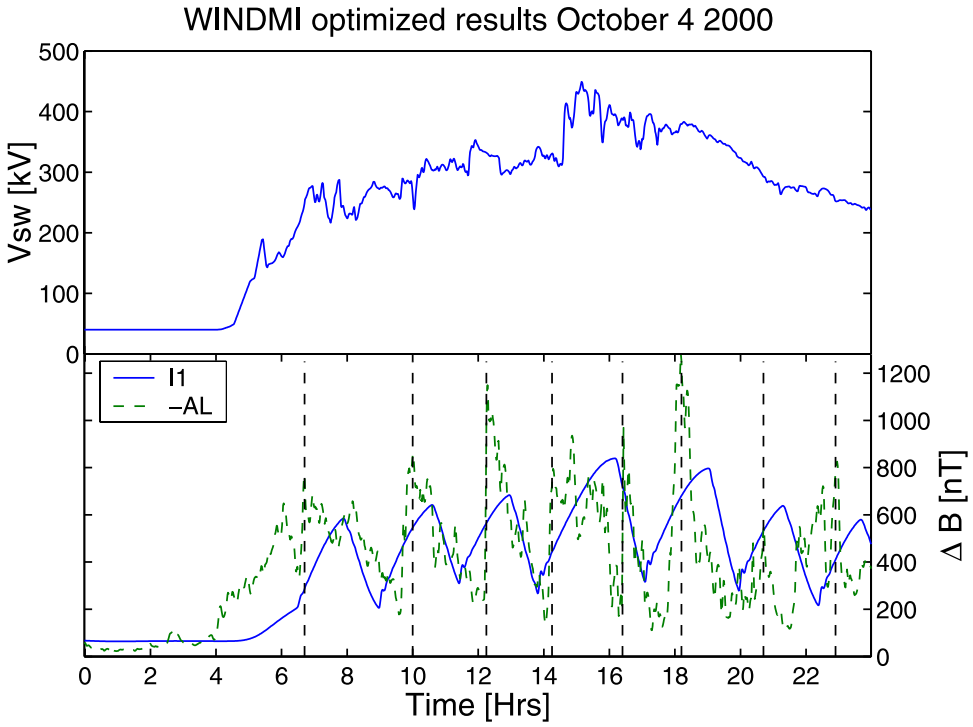

Figure 16. Details of the *AL* prediction during 4 October 2000 with optimized parameters using the rectified input voltage showing the sawtooth (substorm) activity predicted by the WINDMI model. The substorms have roughly the correct period and number, but the timing is not accurate.

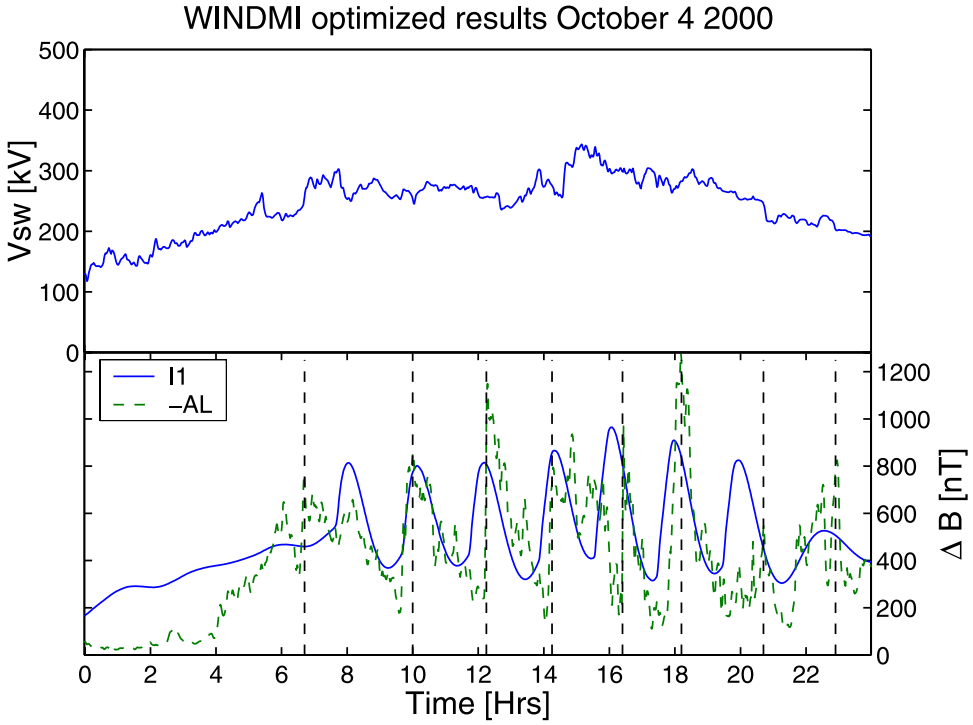

Figure 17. Details of the *AL* prediction during 4 October 2000 with optimized parameters using the Siscoe input voltage showing the substorm activity predicted by the model. The sawteeth are qualitatively different from that of the rectified driver in Figure 16.

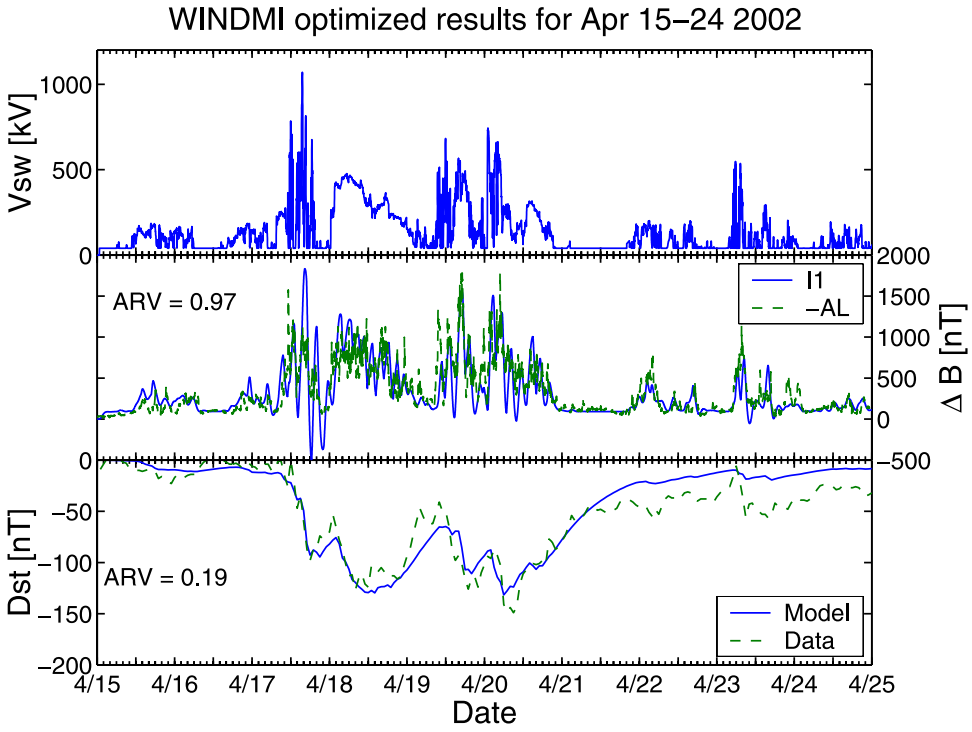

Figure 18. The 15–24 April 2002 optimized using the rectified input voltage. The *Dst* ARV of 0.19 is significantly improved over the rectified nominal output. The sawteeth on 18 April are predicted better with the optimized model than with the nominal model in Figure 12.

2100 UT 4 October, the Siscoe driver optimized solution follows the data to within a few nT, while the rectified driver underestimates the data by about 15–20 nT. This is due to active B_y^{IMF} levels having a role in the Siscoe driver, compared to the rectified driver which only becomes active when B_z^{IMF} is southward. At the end of initial phase 4 October 2100 UT, both solutions do not descend to −143 nT in the *Dst*; the Siscoe solution is under the data by 48 nT, and the rectified driver is under the data by 56 nT.

[81] During the main phase between 4 October 2100 UT to 5 October 1400 UT, the rectified optimized solution performs best in reproducing the timing and magnitude of the minima. The solution only underestimates the first peak of −175 nT by a few nT, and the second peak of −182 nT by ∼10 nT. The Siscoe optimized solution does not follow the minima and maxima as well as the rectified optimized solution because it underestimates the peaks by 30 nT and 60 nT, respectively. Finally, during the recovery phase, the optimized rectified solution decays following the data closely to 0400 UT 6 October and then underestimates the data by 15–25 nT through the end of the recovery phase. The Siscoe optimized solution decays too rapidly and deviates by 30–40 nT from the data throughout the recovery phase.

[82] In the *AL* prediction, the rectified optimal solution in Figure 14 predicts five peaks during the series of sawteeth on 3 October and eight peaks on 4 October. It captures the first large spike on 5 October of −1938 nT at 0651 UT but underestimates it by about 540 nT. During the inactive period between the two peaks on 5 October, it undershoots by −800 nT. In predicting the second large peak of −2790 nT at 1210 UT 5 October, it underestimates the data by about 1700 nT and is delayed by 1 hour.

[83] In comparison, the Siscoe optimized solution in Figure 15 captures six peaks for the first series of sawteeth on 3 October, but on 4 October it captures eight peaks. It only underestimates the first *AL* surge on 5 October by 390 nT, but predicts it 12 min early. The Siscoe optimized solution *AL* predicts an undershoot in the inactive period between the two peaks on 5 October of −250 nT. It also underestimates the second peak on 5 October by 1450 nT but predicts the peak at the right time.

[84] Magnified plots of the *AL* activity on 4 October 2000 are shown in Figures 16 and 17. Both optimized solutions capture the correct number of oscillations and roughly give the correct periods, but the timing of each oscillation is not accurate. Qualitatively, the Siscoe solution captures the rise to maxima of each oscillation better, while the rectified solution captures the decrease to minima of each oscillation better.

[85] The average input power to the geotail from $V \times I$ during the 5 day period is 2.1 TW using the rectified input. There are large surges in the input power to the ionosphere during the *AL* peaks on 5 October 0651 and 1210 UT of 1.45 TW and 0.66 TW, respectively. We plan to study the probability distributions of these surges and consider the nonlinear precipitation-enhanced Robinson conductivity in a future work. Large power surges of shorter durations also occur into the inner magnetosphere due to losses from periods of enhanced parallel mass flows.

6.2. Event of 15–24 April 2002

[86] The results from optimization for the 15–24 April 2002 storm are shown for the rectified driver in Figure 18 and for the Siscoe driver in Figure 19. The *AL* activity on 18 April during the sawteeth oscillations is shown for each

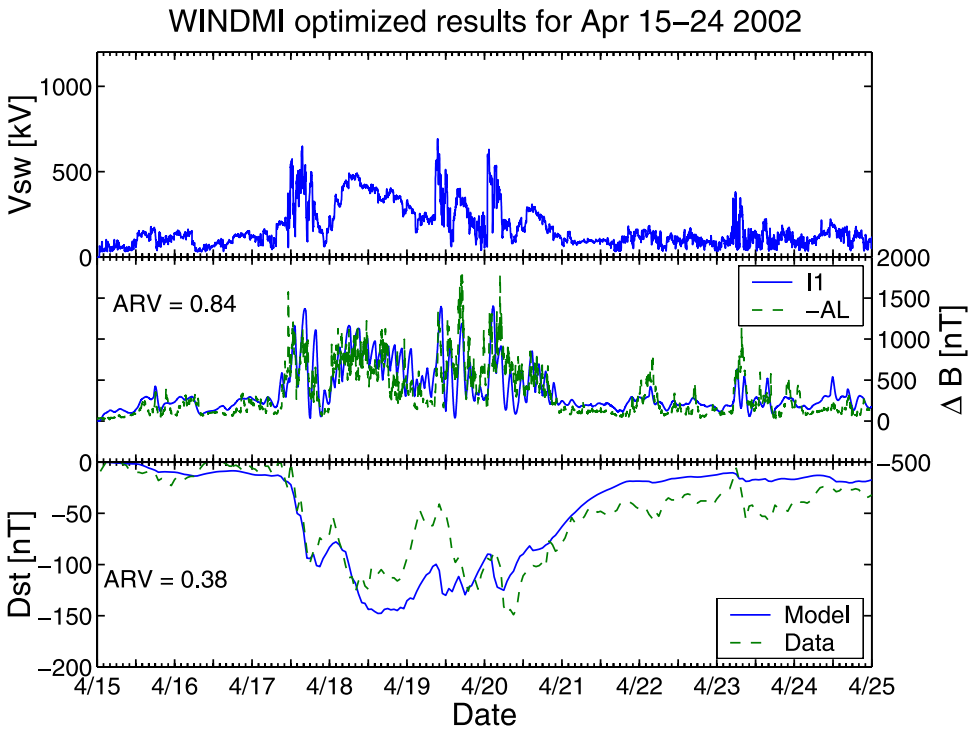

Figure 19. The 15–24 April 2002 optimized using the Siscoe input voltage. Both the *AL* and *Dst* predictions have improved over the nominal output. This result gives the best *AL* ARV prediction of 0.84.

driver in Figures 20 and 21. Very similar results to the October 2000 storm are obtained as far as the comparison between the two input drivers are concerned. The *Dst* performance is better with the rectified input, while the *AL* prediction is better with the Siscoe input.

[87] The Siscoe optimized solution improves in ARV measures for both the *AL* and *Dst* prediction. The rectified

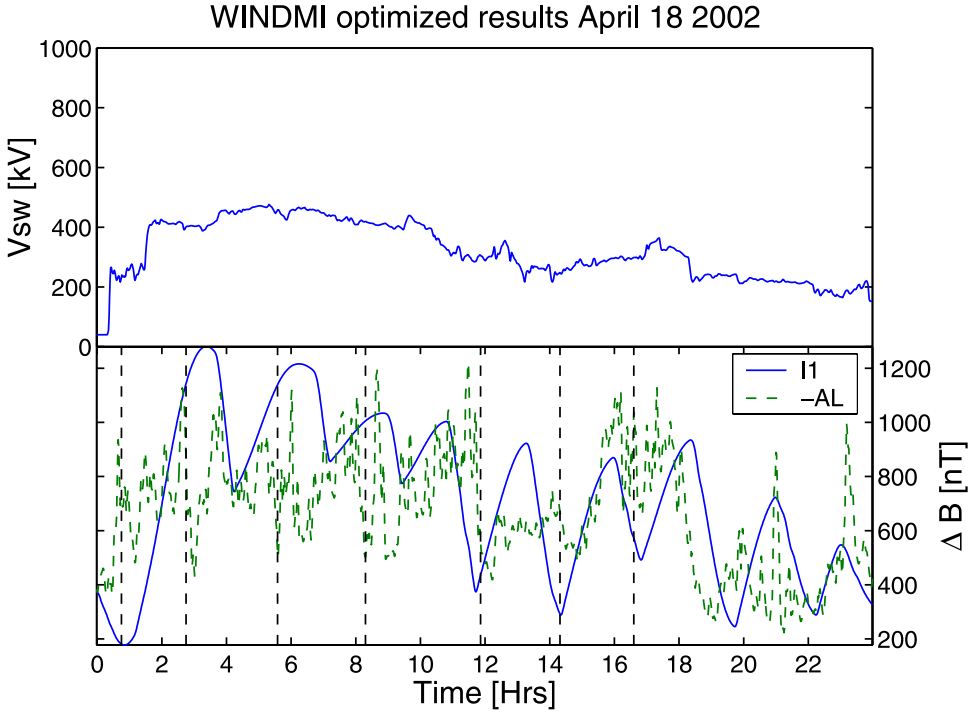

Figure 20. Details of the *AL* prediction on 18 April 2002 with the optimized parameters using the rectified input voltage showing the substorm activity predicted by the model. Although the average period for the oscillations are roughly correct (2 $\sim$ 3 hours), their number and timing do not match the data well.

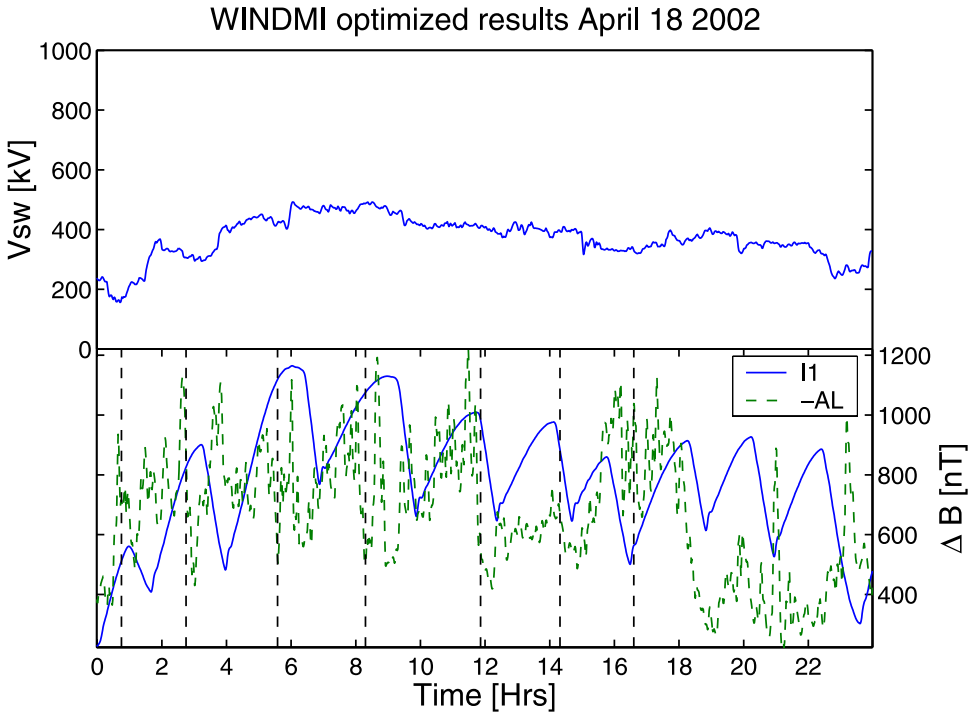

Figure 21. Details of the *AL* prediction on 18 April 2002 with the optimized parameters using the Siscoe input voltage showing the sawtooth (substorm) activity predicted by the model. The model peaks match the data well up to 1152 UT; thereafter the troughs match better.

optimal solution shows improvement in the *Dst* ARV going from 0.32 to 0.19 but does not change significantly in the *AL* ARV, going from 0.96 to 0.97. The *Dst* prediction during the initial phase from 0000 UT 15 April to 0800 UT 18 April are very good and nearly identical with both drivers under nominal or optimized conditions. The nominal Siscoe solution gives the best prediction during this period, matching the maximum of −53 nT at 0100 UT 18 April exactly.

[88] The Siscoe driver nominal and optimal solutions decay too slowly in the period 0800 UT 18 April to 0600 UT 19 April, in the earlier part of the main phase. They overestimate the *Dst* prediction during this period by 30–35 nT. In contrast, the rectified driver nominal and optimal solutions predict the *Dst* very well during the same period. *Liemohn et al.* [2007] argue that the reason that predictions of *Dst* on 18 April 2002 using observed geosynchronous plasma densities fall well short of the measured *Dst* is the due to the weak source populations for the ring current. Ring current models do not represent the enhanced convection thought to be associated with sawtooth events [*Borovsky et al.*, 2007]. At the same time, *Dst* prediction schemes like *Burton et al.* [1975] and *O'Brien and McPherron* [2000] based on B_z^{IMF} values alone overpredict the *Dst* during the sawtooth intervals possibly because they do not take into account the weak ring current source population. This implies that the ring current during sawtooth events may have unusual characteristics in which fewer particles are accelerated to higher energies to create the observed current intensity. The WINDMI model injects energy into the ring current from the plasma sheet but does not take into account changes in the plasma sheet density. Modeling the sources and sinks of plasma sheet density is a complicated problem for future studies.

[89] During the main phase, three peaks occur, the first, −126 nT at 1900 UT 19 April, the second, −148 nT at 0700 UT 20 April, and the third, −149 nT at 0900 UT 20 April. The rectified optimal solution performs best and reproduces two of the peaks in timing but underestimates them both in strength by 10–15 nT. The Siscoe optimized solution has bad timing but captures the first peak in magnitude, while underestimating the second peak by 30 nT. Both the Siscoe and rectified optimal solutions miss the third peak.

[90] The optimized rectified solution behaves best over the earlier part of the recovery phase, decaying at the same rate and about the same levels over the period 1000 UT 20 April to 0900 UT 21 April. Toward the end of the recovery phase past 0000 UT 22 April, all the solutions underestimate the *Dst* activity by 10–30 nT. The overall *Dst* prediction is best with the optimized rectified solution, with an ARV of 0.19.

[91] The best ARV of 0.84 is returned by the optimized Siscoe solution for the *AL* prediction. On 17 April, during the first shock event, the Siscoe optimal solution predicts three peaks in the *AL* signature quite accurately in timing and does not undershoot like the rectified optimal solution. During the period of strong activity between 19 April and 20 April associated with the second shock, two large surges occur. The first surge reaches a maximum of 1824 nT at 1648 UT 19 April and the second surge reaches a maximum of 1851 nT at 0451 UT 20 April. Both these peaks are captured by the nominal as well as the optimized solutions, but the rectified optimized solution does best, only underestimating the first peak by about 210 nT and the second by 490 nT. The Siscoe solution does not do as well as the rectified solution, it captures the peaks in timing but underestimates the strength of the first peak by about 600 nT and the second peak by 875 nT.

[92] The calculated average power deposited to the ionosphere during the *AL* peak on 17 April 1100 UT is 1.5 TW due to the first CME. The effects of the second CME yielded two peaks, 19 April 1648 UT and 20 April 0451 UT, and the average power deposited is 1.25 TW and 0.91 TW, respectively. The final CME produced a peak in the *AL* on 23 April 0741 UT, with the average power deposited to the ionosphere being 0.25 TW.

[93] The sawteeth activity during the magnetic cloud event is shown in Figures 20 and 21. The Siscoe optimized solution captures the first *AL* sawtooth peak at 0045 UT 18 April while the rectified optimized solution does not. On the other hand, the rectified solution does better toward the end of the day, capturing the *AL* peaks at 2047 UT 18 April as well as the peak in the *AL* right after it at approximately 2300 UT 18 April. Overall, the earlier oscillations are captured better by the Siscoe optimized solution, while the later oscillations are captured better by the rectified solution.

7. Summary and Discussion

[94] A plasma physics network model called WINDMI-RC is used to calculate the eight energy components in the solar wind driven magnetosphere-ionosphere-ring current system. The parameter vector **P** has 18 physical parameters of the system that are estimated a priori within realizable ranges from the physics of the system. A genetic algorithm multiobjective optimization routine is then used to find optimal models for given historical storm-substorm events. The 3–7 October 2000 storm and the 15–24 April 2002 large geomagnetic storm with similar auroral activity are examined in detail. Key features and conclusions are the following:

[95] 1. The internal trigger for unloading plasma pressure allows the model to represent adequately the recurrent substorm and sawtooth oscillations, with the timing and relative amplitudes in rough agreement with the *AL* westward auroral magnetic index and LANL geosynchronous spacecraft energetic particle flux data. External solar wind triggers are not required. The model does not have an explicit solar wind trigger mechanism of the type give by *Lyons* [1995] and *Lyons et al.* [2005]. The Lyons northward turning switch has been experimented with and its effect will be discussed in future work.

[96] 2. For both the 3–7 October 2000 and 15–24 April 2002 storms the model describes the features driven by the solar wind data through the complex M-I system. The magnetic cloud and interplanetary shock effects are clearly expressed in the predicted output geomagnetic indices.

[97] 3. Two alternative formulations of the solar wind dynamo driving voltage are used, the rectified vB_s and the voltage of *Siscoe et al.* [2002b] that takes into account the compression/expansion of the magnetosphere due to the solar wind dynamic pressure.

[98] 4. We optimize the physical parameters to achieve low average relative variance (ARV) for the *AL* and *Dst* outputs with a multiobjective genetic algorithm procedure. While the results for the optimized models driven by the rectified driver and the pressure modulated driver are similar, for both storms the rectified driver gives a more accurate prediction for the *Dst*, and the Siscoe pressure modulated driver gives a more accurate prediction of the westward auroral electrojet index.

Table 4. Storm Key Optimized Parameters for 15–24 April 2002 Obtained Through Genetic Algorithm Optimization

Parameter	GA Rectified	GA Siscoe
L, H	64	52
C, F	110,000	140,000
Σ, mho	10	8.8
u_0	4.3×10^{-9}	2.4×10^{-9}
I_c, A	1×10^7	1.1×10^7
Σ_I, mho	4	2.2
τ_{rc}, s	62,000	45,000
A_{eff}, m^2	9.7×10^{13}	10×10^{13}

[99] 5. Comparison of the optimal physical parameters for the two storms in Tables 3 and 4 with the nominal physics values in Tables 1 and 2 shows the largest deviation for C determines the mass density and magnetic field in the central plasma sheet. The average C value is 10^5 F from Tables 3 and 4 which is two times that of Table 1. This suggests that there may be a high O^+ mass density content or a lower mean value of the B_z in the central plasma sheet during storm times.

[100] 6. The optimal values derived for the parameters yield information on the size and state of the magnetospheric and ionospheric plasmas that may be used in future studies. The GA optimized WINDMI model improves our understanding of the flow of power from the solar wind dynamo through the numerous reservoirs the model makes specific. The GA optimized parameters gives a theoretical picture of the plasma and scale sizes of the M-I system.

[101] 7. WINDMI only underestimates minimum values of the *Dst* index by 5–15 nT in both of the magnetic storm events when using the rectified driver. The Siscoe driver underestimates more, by about 30–60 nT. This is likely due to the changing plasma sheet density not represented in WINDMI as the magnetosphere cycles between shock/sheath-driven and CME-driven activity throughout the events. The former tends to be associated with high plasma sheet density values while the later with low ones.

Appendix A: Single and Multiobjective Genetic Algorithm Implementation

[102] The implementation here is a variant of the simple genetic algorithm [*Coley*, 2003]. More elaborate schemes with multiple crossover locations, generation dependent mutation parameters, elitism, and fitness proportional selection have not yet been explored. The basis for the multiobjective genetic algorithm scheme is the single-objective method, which will be described first.

[103] The variable coefficients in the WINDMI model are L, M, C, Σ, Ω_{cps}, u_0, I_c, A_{eff}, B_{tr}, L_y, τ_E, $\tau_{||}$, L_I, C_I, Σ_I, L_2, R_{prc}, R_{A2}, τ_{rc}, and α. These parameters are constrained to maximum and minimum physically realizable and allowable values and combined to form a 18-dimensional search space $S \subset \mathbb{R}^{18}$ over which optimization is performed. A single set of parameters corresponds to a point $s \in S$.

[104] An initial random generation of size $N = 2^k$ parameter sets $G_1 = \{s^i \in S;\ i = 1..N\}$ is created, and each set s^i is used to solve the set of ODEs for a particular storm. A

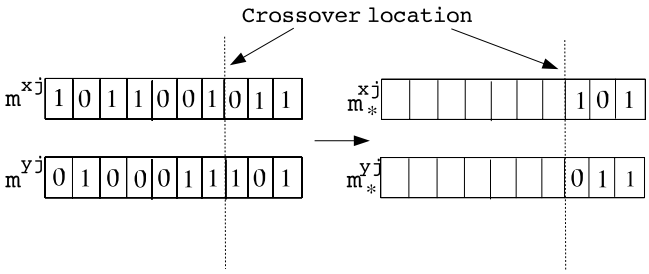

Figure A1. Illustration of the genetic algorithm crossover process. After crossover, a mutation operator examines every bit of each offspring and flips a bit based on a mutation probability parameter $\mu = 0.15$.

fitness metric is evaluated for each s^i and the set G_1 is rearranged in descending order with respect to the fitness metric. The best $N/2$ parameter sets are retained to form a set G_1^{best} while the remaining $N/2$ sets are discarded. We then proceed to create a set G_2 with N elements. This is done by first combining the $N/2$ members of G_1^{best} to produce a set G_1^{ofs} of $N/2$ offspring. The offspring are created by a random pairing of sets in G_1^{best}. Each pair of sets produce two offspring by sharing parameter values between them through a crossover and mutation procedure, which will be explained below. The collection G_1^{best} G_1^{ofs} then forms a new generation of N parameter sets G_2, and the selection process is continued until satisfactory convergence to a minimized solution is obtained for some generation G_M.

[105] To produce the first generation G_1, we first define the minimum and maximum values that each parameter s^{ij} is allowed to take. Here $i = 1..N$ is the index over the number of parameter sets in G_1 and $j = 1..18$ is the index over the number of parameters in each parameter set. The minimum and maximum values are denoted respectively as $s^{ij}_{\min}$ and $s^{ij}_{\max}$. We choose a resolution n and write each s^{ij} as

$$s^{ij} = s^{ij}_{\min} + \left(\frac{s^{ij}_{\max} - s^{ij}_{\min}}{2^n}\right) m^{ij} \tag{A1}$$

where m^{ij} is an integer that can take values from 0 through $2^n - 1$. Each parameter is then set by randomly choosing m^{ij} for all j to construct each s^i and then for all i to construct G_1.

[106] The biological process of natural selection is accomplished by simply retaining the best half of a generation based on the fitness metric, as mentioned before. To perform crossover at the qth generation, we first randomly pair off the best parameter sets in G_q^{best}. Given a pair of parameter sets s^x and s^y, we produce two offspring as follows. For every j from 1 to 18, we convert the numbers m^{xj} and m^{yj} into their n-bit binary representations. Next we randomly choose a crossover location at some pth bit, and swap all the bits to the right of the pth bit between m^{xj} and m^{yj}. Two new binary numbers m^{xj}_* and m^{yj}_* are thus produced. The crossover procedure is illustrated in Figure A1.

[107] Some parameters are purposely mutated by a random process to take values that are in range but not necessarily fit. This mutation process ensures that the search space is thoroughly explored and convergence to a local optimum does not occur. On the basis of a small mutation probability parameter $\mu = 0.15$, each of the bits of the numbers m^{xj}_* and m^{yj}_* may now be reversed. This is the mutation part of the process. After the mutation procedure, the binary numbers are converted back to their integer representations. The crossover and mutation are repeated for all j and the result is two offspring sets s^x_* and s^y_* that will be members of G_q^{ofs}. Continuing in this manner, we construct the generation G_{q+1} composed of G_q^{best} and G_q^{ofs}.

[108] If we want to use a combination of objective functions to evaluate the fitness of a particular parameter set, we need to turn to a multiobjective optimization algorithm. The method is based on the concept of nondominance between any two solutions, which is defined below. We first select M objective functions, that is, $k = 1,2,3\ldots M$. At each generation, we form a family of parameter sets N_D with the following two properties [*Deb*, 2001]: (1) Any two solutions of N_D must be nondominated with respect to each other. (2) Any solution not belonging to N_D is dominated by at least one member of N_D. A solution s^1 is said to dominate another solution s^2, if (1) s^1 is no worse than s^2 in all M objectives, (2) s^1 is strictly better than s^2 in at least one objective.

[109] When we have searched the entire space of solutions and have a final nondominated set N_D after some number of generations, we obtain what is referred to as the pareto-optimal set, which is a set of nondominated family of solutions that are better than all other solutions in the search space and are comparable to each other in fitness, through the dominance relation.

[110] **Acknowledgments.** This work was partially supported by NSF grant ATM-0539099. J. Kozyra would like to acknowledge support for this work under NASA grant NNG05GJ89G and NSF grant ATM-0402163. The authors also wish to acknowledge Los Alamos National Labs for the LANL satellite data and Gang Lu at NCAR for the 15–24 April 2002 storm *AL* and *Dst* geomagnetic indices. The SOHO LASCO CME Catalog is generated and maintained by NASA and Catholic University of America in cooperation with the Naval Research Laboratory. We acknowledge the use of data from the ACE, Geotail, and LANL satellites. The solar wind plasma and magnetic field data were obtained from ACE at NASA's CDAWeb site. The geomagnetic indices used were obtained from the WDC for Geomagnetism, Kyoto.

[111] Amitava Bhattacharjee thanks Ruth Skoug and A. Surjalal Sharma for their assistance in evaluating this paper.

References

Bargatze, L. F., R. L. McPherron, J. Minamora, and D. Weimer (2005), A new interpretation of Weimer et al.'s solar wind propagation delay technique, *J. Geophys. Res.*, *110*, A07105, doi:10.1029/2004JA010902.

Blanchard, G., and R. McPherron (1993), A bimodal representation of the response function relating the solar wind electric field to the AL index, *Adv. Space Res.*, *13*(4), 71.

Borovsky, J. E., R. J. Nemzek, C. W. Smith, R. M. Skoug, and C. R. Clauer (2007), The solar wind driving of global sawtooth oscillations and periodic substorms: What determines the periodicity?, *Ann. Geophys*, in press.

Burton, R. K., R. L. McPherron, and C. T. Russell (1975), An empirical relationship between interplanetary conditions and Dst, *J. Geophys. Res.*, *80*, 4204–4214.

Cane, H. V., and I. G. Richardson (2003), Interplanetary coronal mass ejections in the near-Earth solar wind during 1996–2002, *J. Geophys. Res.*, *108*(A6), 1156, doi:10.1029/2002JA009817.

Coley, D. (2003), *An Introduction to Genetic Algorithms for Scientists and Engineers*, World Sci., Tokyo.

Deb, K. (2001), *Multiobjective Optimization Using Evolutionary Algorithms, Wiley Intersci. Ser. in Syst. and Opt.*, 1st ed., John Wiley, Hoboken, N. J.

Dessler, A., and E. N. Parker (1959), Hydromagnetic theory of geomagnetic storms, *J. Geophys. Res.*, *64*, 2239–2259.

Doxas, I., W. Horton, W. Lin, S. Seibert, and M. Mithaiwala (2004), A dynamical model for the coupled inner magnetosphere and tail, *IEEE Trans. Plasma Sc.*, *32*(4), 1443–1448.

Gopalswamy, N., S. Yashiro, O. St. Cyr, G. Lawrence, M. L. Kaiser, J. B. Gurman, and R. A. Howard (2002), Solar, interplanetary, and geospace disturbances associated with the April 2002 coronal mass ejections, *Eos Trans. AGU*, *83*(47), Fall Meet. Suppl., Abstract SA12A-02.

Henderson, M. (2004), The May 2–3, 1986 CDAW-9C interval: A sawtooth event, *Geophys. Res. Lett.*, *31*, L11804, doi:10.1029/2004GL019941.

Henderson, M. G., G. D. Reeves, R. Skoug, M. F. Thomsen, M. H. Denton, S. B. Mende, T. J. Immel, P. C. Brandt, and H. J. Singer (2006), Magnetospheric and auroral activity during the 18 April 2002 sawtooth event, *J. Geophys. Res.*, *111*, A01S90, doi:10.1029/2005JA011111.

Horton, W., and I. Doxas (1996), A low-dimensional energy-conserving state space model for substorm dynamics, *J. Geophys. Res.*, *101*(A12), 27,223–27,237.

Horton, W., and I. Doxas (1998), A low-dimensional dynamical model for the solar wind driven geotail-ionosphere system, *J. Geophys. Res.*, *103*(A3), 4561–4572.

Horton, W., and M. Pekker (1998), Magnetic energy storage and the nightside magnetosphere-ionosphere coupling, *J. Geophys. Res.*, *25*(21), 4083–4086.

Horton, W., and T. Tajima (1991), Collisionless conductivity and stochastic heating of the plasma sheet in the geomagnetic tail, *J. Geophys. Res.*, *95*(A9), 15,811–15,829, doi:10.1029/91JA01014.

Horton, W., R. S. Weigel, D. Vassiliadis, and I. Doxas (2003), Substorm Classification with the WINDMI Model, *Nonlinear Proc. Geophys.*, *10*, 363.

Horton, W., M. Mithaiwala, E. Spencer, and I. Doxas (2005a), WINDMI: A family of physics network models for storms and substorms, in *Multi-Scale Coupling of Sun-Earth Processes*, edited by A. Lui, Y. Kamide, and G. Consolini, Elsevier, New York.

Horton, W., E. Spencer, I. Doxas, and J. Kozyra (2005b), Analysis of the October 3–7 2000 GEM storm with the WINDMI Model, *Geophys. Res. Lett.*, *32*, L22102, doi:10.1029/2005GL023515.

Horton, W., M. L. Mays, and E. Spencer (2007), Physics modeling of storms and substorms with solar wind data, in *Proceedings of the Eighth International Conference on Substorms (ICS-8)*, edited by M. Syrjäsuo and E. Donovan, pp. 93–98, Univ. of Calgary, Alberta, Canada, in press.

Huang, C., J. Foster, G. Reeves, G. Le, H. Frey, C. Pollock, and J.-M. Jahn (2003a), Periodic magnetospheric substorms: Multiple space-based and ground-based observations, *J. Geophys. Res.*, *108*(A11), 1411, doi:10.1029/2003JA009992.

Huang, C.-S., G. Reeves, J. Borovsky, R. Skoug, Z. Pu, and G. Le (2003b), Periodic magnetospheric substorms and their relationship with solar wind variations, *J. Geophys. Res.*, *108*(A6), 1255, doi:10.1029/2002JA009704.

Kivelson, M., and C. Russell (Eds.) (1995), *Introduction to Space Physics*, Cambridge Univ. Press, New York.

Liemohn, M. W., J. U. Kozyra, A. J. Ridley, M. F. Thomsen, M. G. Henderson, P. C. Brandt, and D. G. Mitchell (2007), Modeling the ring current response to a sawtooth oscillation event, *J. Atmos. Sol. Terr. Phys.*, *69*, 67–76.

Lyons, L. (1995), A new theory for magnetospheric substorms, *J. Geophys. Res.*, *100*(A10), 19,069–19,081.

Lyons, L. R., D.-Y. Lee, C.-P. Wang, and S. B. Mende (2005), Global auroral responses to abrupt solar wind changes: Dynamic pressure, substorm, and null events, *J. Geophys. Res.*, *110*, A08208, doi:10.1029/2005JA011089.

Manoharan, P. K., N. Gopalswamy, S. Yashiro, A. Lara, G. Michalek, and R. A. Howard (2004), Influence of coronal mass ejection interaction on propagation of interplanetary shocks, *J. Geophys. Res.*, *109*, A06109, doi:10.1029/2003JA010300.

Ober, D. M., N. C. Maynard, and W. J. Burke (2003), Testing the Hill model of transpolar potential saturation, *J. Geophys. Res.*, *108*(A12), 1467, doi:10.1029/2003JA010154.

O'Brien, T. P., and R. L. McPherron (2000), An empirical phase space analysis of ring current dynamics: Solar wind control of injection and decay, *J. Geophys. Res.*, *105*, 7707–7720.

Ohtani, S., M. Nosé, G. Rostoker, H. Singer, A. T. Y. Lui, and M. Nakamura (2001), Storm-substorm relationship: Contribution of the tail current to Dst, *J. Geophys. Res.*, *106*, 21,199–21,210.

Reeves, G. (2003), Image, polar, and geosynchronous observations of substorm and ring current ion injection, in *Disturbances in Geospace: The Storm-Substorm Relationship*, *Geophys. Monogr. Ser.*, vol. 142, edited by A. S. Sharma, Y. Kamide, and G. S. Lakhina, pp. 91–101, AGU, Washington, D. C.

Reiff, P. H., and J. G. Luhmann (1986), Solar wind control of the polar-cap voltage, in *Solar Wind-Magnetosphere Coupling*, edited by Y. Kamide and J. A. Slavin, pp. 453–476, Terra Sci., Tokyo.

Sckopke, N. (1966), A general relation between the energy of trapped particles and the disturbance field near the Earth, *J. Geophys. Res.*, *71*, 3125.

Siscoe, G. L., N. U. Crooker, and K. D. Siebert (2002a), Transpolar potential saturation: Roles of region-1 current system and solar wind ram pressure, *J. Geophys. Res.*, *107*(A10), 1321, doi:10.1029/2001JA009176.

Siscoe, G. L., G. M. Erickson, B. U. O. Sonnerup, N. C. Maynard, J. A. Schoendorf, K. D. Siebert, D. R. Weimer, W. W. White, and G. R. Wilson (2002b), Hill model of transpolar potential saturation: Comparisons with MHD simulations, *J. Geophys. Res.*, *107*(A6), 1075, doi:10.1029/2001JA000109.

Tsyganenko, N. A., and A. V. Usmanov (1982), Determination of the magnetospheric current system parameters and development of experimental geomagnetic field models based on data from IMP and HEOS satellites, *Planet. Space Sci.*, *30*, 985–998.

Turner, N. E., D. N. Baker, T. I. Pulkkinen, and R. L. McPherron (2000), Evaluation of the tail current contribution to Dst, *J. Geophys. Res.*, *105*, 5431–5440.

Wang, Y., P. Ye, S. Wang, and X. Xue (2003), An interplanetary cause of large geomagnetic storms: Fast forward shock overtaking preceding magnetic cloud, *Geophys. Res. Lett.*, *30*(13), 1700, doi:10.1029/2002GL016861.

Weimer, D. R. (2004), Correction to "Predicting interplanetary magnetic field (IMF) propagation delay times using the minimum variance technique, *J. Geophys. Res.*, *109*, A12104, doi:10.1029/2004JA010691.

Weimer, D., D. Ober, N. Maynard, M. Collier, D. McComas, N. Ness, C. Smith, and J. Watermann (2003), Predicting Interplanetary magnetic field (IMF) propagation delay times using the minimum variance technique, *J. Geophys. Res.*, *108*(A1), 1026, doi:10.1029/2002JA009405.

Yoon, P., A. Lui, and M. Sitnov (2002), Generalized lower-hybrid drift instabilities in current sheet equilibrium, *Phy. Plasmas*, *9*(5), 1526–1538.

I. Doxas, Center for Integrated Plasma Studies, University of Colorado, Boulder, CO, USA.

W. Horton and M. L. Mays, Institute for Fusion Studies, University of Texas at Austin, RLM 11.222, Austin, TX, USA.

J. Kozyra, Department of Atmospheric, Oceanic and Space Sciences, University of Michigan, Ann Arbor, MI, USA.

E. Spencer, Center for Space Engineering, Utah State University, 4170 Old Main Hill, Logan, UT 84322, USA.